Helium isotopic textures in Earth's upper mantle

Citation	Graham, D. W., B. B. Hanan, C. Hémond, J. Blichert-Toft, and F. Albarède (2014), Helium isotopic textures in Earth's upper mantle. Geochemistry Geophysics Geosystems, 15, 2048–2074. doi:10.1002/2014GC005264
DOI	10.1002/2014GC005264
Publisher	American Geophysical Union
Version	Version of Record
Terms of Use	http://cdss.library.oregonstate.edu/sa-termsofuse

AGU PUBLICATIONS

Geochemistry, Geophysics, Geosystems

RESEARCH ARTICLE

10.1002/2014GC005264

Helium isotopic textures in Earth's upper mantle

David W. Graham[1], Barry B. Hanan[2], Christophe Hémond[3], Janne Blichert-Toft[4], and Francis Albarède[4]

[1]College of Earth, Ocean, and Atmospheric Sciences, Oregon State University, Corvallis, Oregon, USA, [2]Department of Geological Sciences, San Diego State University, San Diego, California, USA, [3]Domaines Océaniques, Institut Universitaire Européen de la Mer, Place Nicolas Copernic, Plouzané, France, [4]Laboratoire de Géologie de Lyon, Ecole Normale Supérieure de Lyon and Université Claude Bernard Lyon 1, CNRS UMR 5276, Lyon, France

Key Points:
- $^3He/^4He$ along ocean ridges carries information about the upper mantle flow field
- Long-wavelength variations are similar for Indian, Atlantic, and Pacific ridges
- Short length scale variations result from melting of heterogeneous mantle

Supporting Information:
- ReadMe
- AuxiliaryMaterial FS1-FS4
- AuxiliaryMaterial Text1
- AuxiliaryMaterial S1

Correspondence to:
D. W. Graham,
dgraham@coas.oregonstate.edu

Citation:
Graham, D. W., B. B. Hanan, C. Hémond, J. Blichert-Toft, and F. Albarède (2014), Helium isotopic textures in Earth's upper mantle, *Geochem. Geophys. Geosyst.*, *15*, 2048–2074, doi:10.1002/2014GC005264.

Received 24 JAN 2014
Accepted 23 APR 2014
Accepted article online 27 APR 2014
Published online 30 MAY 2014

Abstract We report $^3He/^4He$ for 150 mid-ocean ridge basalt (MORB) glasses from the Southeast Indian Ridge (SEIR). Between 81°E and 101°E $^3He/^4He$ varies from 7.5 to 10.2 R_A, encompassing more than half the MORB range away from ocean island hot spots. Abrupt transitions are present and in one case the full range occurs over ~10 km. Melting of lithologically heterogeneous mantle containing a few percent garnet pyroxenite or eclogite leads to lower $^3He/^4He$, while $^3He/^4He$ above ~9 R_A likely indicates melting of pyroxenite-free or eclogite-free mantle. Patterns in the length scales of variability represent a description of helium isotopic texture. We utilize four complementary methods of spectral analysis to evaluate this texture, including periodogram, redfit, multitaper method, and continuous wavelet transform. Long-wavelength lobes with prominent power at 1000 and 500 km are present in all treatments, similar to hot spot-type spectra in Atlantic periodograms. The densely sampled region of the SEIR considered separately shows significant power at ~100 and ~30–40 km, the latter scale resembling heterogeneity in the bimodal distribution of Hf and Pb isotopes in the same sample suite. Wavelet transform coherence reveals that $^3He/^4He$ varies in-phase with axial depth along the SEIR at ~1000 km length scale, suggesting a coupling between melt production, $^3He/^4He$ and regional variations in mantle temperature. Collectively, our results show that the length scales of MORB $^3He/^4He$ variability are dominantly controlled by folding and stretching of heterogeneities during regional (~1000 km) and mesoscale (~100 km) mantle flow, and by sampling during the partial melting process (~30 km).

1. Introduction

The origin, scale, and survival of mantle heterogeneities, and the link to mantle convection have been of considerable interest for 50 years [e.g., *Gast et al.*, 1964; *Tatsumoto*, 1978; *Polvé and Allègre*, 1980; *Allègre et al.*, 1980; *Zindler et al.*, 1982; *Hart*, 1984; *White*, 1985; *Zindler and Hart*, 1986; *Allègre and Turcotte*, 1986; *Sun and McDonough*, 1989; *Hofmann*, 1997; *Albarède*, 2005; *Anderson*, 2006; *Iwamori et al.*, 2010, and many others]. During the past decade, our understanding of mantle geochemistry has grown tremendously, mainly through the rich picture that is emerging by detailed mapping of isotopic variability in oceanic basalts, which are the partial melting products of the mantle. Computational modeling of mantle dynamics has also begun to quantify the range and distribution of geochemical variability produced during mantle convection and tectonic plate recycling [*Christensen and Hofmann*, 1994; *Kellogg et al.*, 2002, 2007; *Brandenburg et al.*, 2008]. These models emphasize the need to quantify isotopic variability at localities such as mid-ocean ridges and areas of hot spot-ridge interaction, and at length scales that range from dense sampling within individual ridge segments up to regional (ocean basin) scales [*Rubin et al.*, 2009]. There is clear evidence that stretching and folding of upper mantle material during convection [e.g., *Olson et al.*, 1984] produces periodic patterns in mantle heterogeneities that are sampled by melting beneath mid-ocean ridges. Indeed, the spatial patterns in MORB isotope compositions reflect blobs and streaks that originate from both the deep mantle and from tectonically recycled crust and lithosphere [*Gurnis*, 1986a, 1986b; *Agranier et al.*, 2005; *Meyzen et al.*, 2007; *Graham et al.*, 2006; *Hanan et al.*, 2013].

Magmas produced beneath mid-ocean ridges represent our best probes of upper mantle composition and the conditions of melting. Spatial variations in melt generation beneath ridges linked to intrinsic variations in mantle heterogeneity or to lateral variations in mantle temperature are further revealed by the relations between basalt composition and physical attributes of ridges such as axial depth, ridge morphology, and

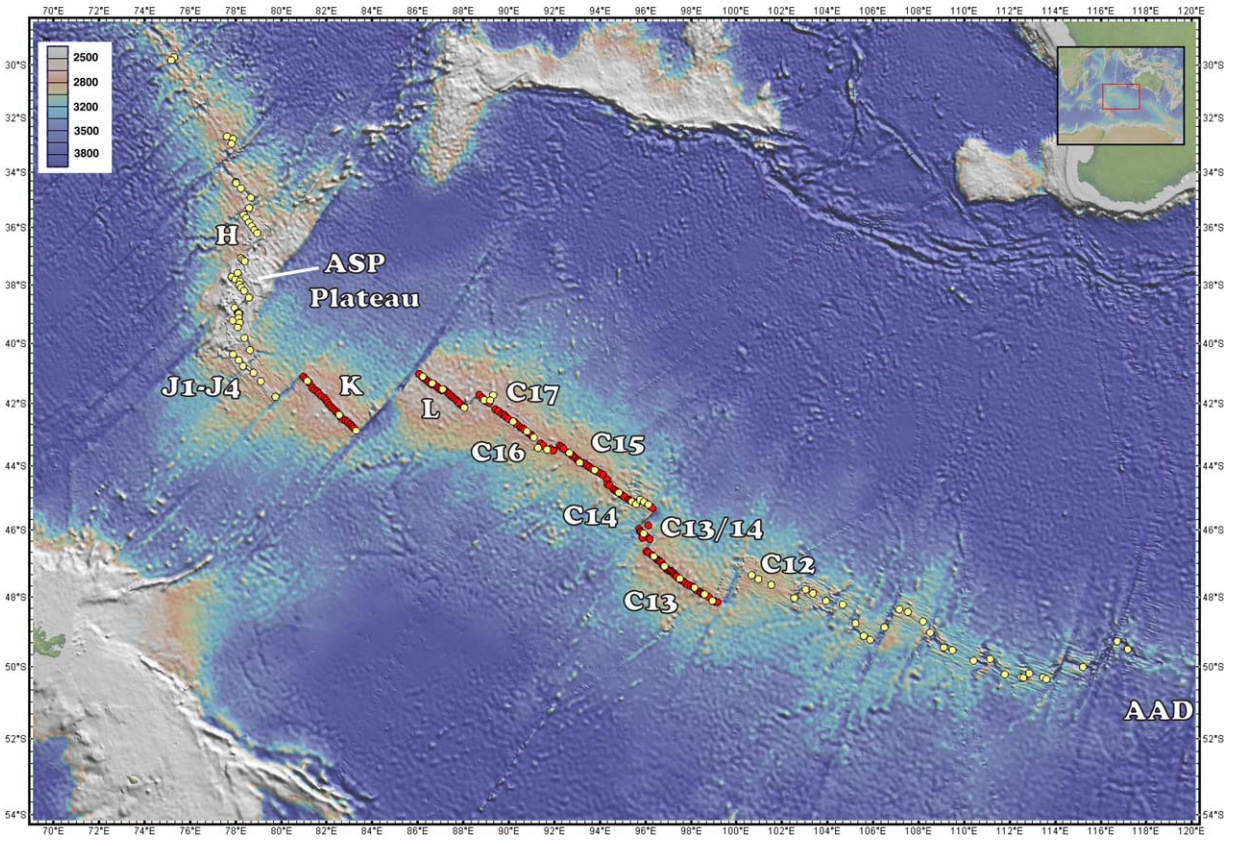

Figure 1. Location map of basalt glasses from the Southeast Indian Ridge analyzed for He isotopes. Individual ridge segments, the Amsterdam-St. Paul (ASP) Plateau, and the Australian-Antarctic Discordance (AAD) are indicated. Red circles are the GEISEIR I and II sample suites from this study. Other samples in yellow have $^{3}He/^{4}He$ data reported in *Graham et al.* [1999, 2001], *Mahoney et al.* [2002], and *Nicolaysen et al.* [2007]. The base map was made using GeoMapApp (http://www.marine-geo.org/geomapapp), which is supported by the National Science Foundation and internal funding from Lamont-Doherty Earth Observatory.

the depths of seismically imaged magma lenses [*Klein and Langmuir*, 1987; *Shen and Forsyth*, 1995; *Rubin et al*., 2009; *Russo et al*., 2009; *Carbotte et al*., 2013]. Despite the rich picture of upper mantle dynamics emerging from detailed isotope studies of MORBs, the characteristic scales of mantle heterogeneity and their linkage to mantle convection and melting remain poorly understood for large sections of the mid-ocean ridge system. The best-characterized region to date is the northern Mid-Atlantic Ridge [*Agranier et al*., 2005], especially where the MAR crosses the Iceland hot spot and its geologic features can be sampled at very high resolution [*Maclennan et al*., 2003; *Shorttle and Maclennan*, 2011]. The fast-spreading East Pacific Rise between ~9°N and 10°N also stands in sharp contrast to the rest of the mid-ocean ridge system in terms of its dense sampling, although the overall length sampled at high resolution is relatively short (~100 km). For much of the mid-ocean ridge system, our appreciation of mantle heterogeneity and melting at length scales shorter than ridge segmentation scales remains modest, mostly due to inadequate sampling density.

This study describes $^{3}He/^{4}He$ variations along the intermediate spreading rate Southeast Indian Ridge (SEIR), focusing primarily on the region between 81°E and 100°E. The SEIR contains significant along-axis physical and chemical variability that can be used to constrain mantle melting and source lithology [e.g., *Russo et al*., 2009]. It also samples the Indian Ocean upper mantle, which is known to be isotopically distinct from the mantle beneath the Pacific and North Atlantic [*Dupré and Allègre*, 1983; *Hamelin et al*., 1986; *Hart*, 1984; *Dosso et al*., 1988; *Mahoney et al*., 2002]. The SEIR stretches from the Rodrigues Triple Junction (25.6°S, 70.1°E) to the Macquarie Triple Junction (62°S, 151°E; Figure 1). Between 76°E and 78°E it crosses the Amsterdam-St. Paul Plateau (ASP), a pronounced bathymetric swell associated with relatively hot mantle upwelling beneath Amsterdam and St. Paul islands, while between 120°E and 128°E it crosses the

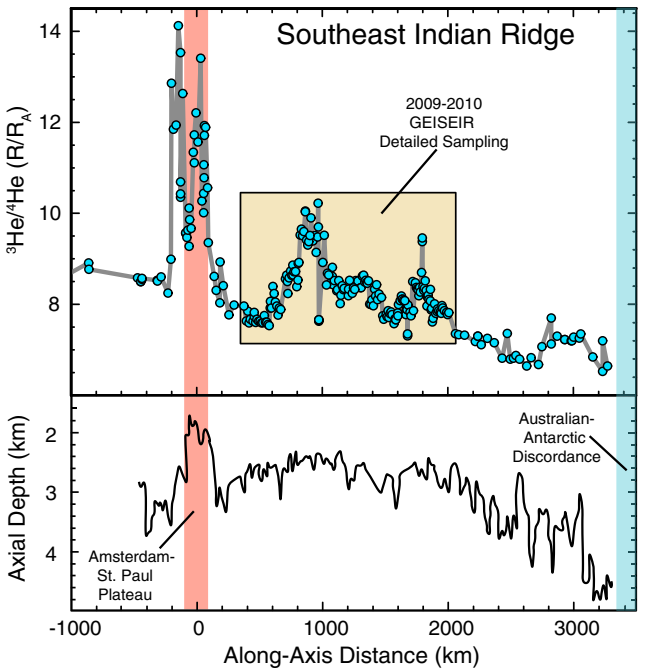

Figure 2. Variations along the Southeast Indian Ridge in $^3He/^4He$ (R/R_A) and axial depth (km). Data sources are the same as for Figure 1. Analytical uncertainties are smaller than the size of the data points. The highlighted box outlines the GEISEIR I and II sampling areas between 81°E and 100°E (n = 175 sample locations, for segments K, L, and C13–C17). Along-axis distance in km is calculated from the pole of plate rotation (13.2°N, 38.2°E) and is expressed relative to the location of St. Paul Island (38.70°S, 77.55°E).

Australian-Antarctic Discordance (AAD), a region of deep bathymetry (>4000 m) associated with relatively cold mantle and low melt production. Notably, over a distance of ~2500 km, between 86°E and 120°E, there is a regular eastward decrease in axial depth from 2300 to 5000 m, and a morphological transition from axial high to axial valley due to decreasing melt production rate and crustal thickness. This depth gradient occurs at intermediate and uniform spreading rate (68–75 mm/yr full rate) and in the absence of large transform offsets and nearby mantle hot spots. Axial depth and ridge morphology encompass most of the global range for spreading ridges away from hot spots, making the SEIR a regional-scale analogue of the 60,000 km long global ocean ridge system. Detailed geophysical surveys have revealed three axial morphological zones between 81°E and 118°E. Most ridge segments in the western zone (K, L, and C17–C13, which recently were resampled and are the focus of the current study; Figure 1) have axial-high morphology, similar in dimension and shape to segments of the fast-spreading East Pacific Rise [*Cochran et al*., 1997; *Sempéré et al*., 1997; *Baran et al*., 2005]. Segments C12-C4 to the east have a transitional morphology typical of other intermediate-spreading ridges.

Earlier work by *Graham et al*. [1999, 2001] discovered localized peaks in $^3He/^4He$ (and Fe8, a proxy for the depth of mantle melting) [*Klein and Langmuir*, 1987] having basal widths between 200 and 500 km that are superimposed on a long-wavelength west-to-east decrease in $^3He/^4He$ (Figure 2). These helium isotope peaks are most prominent near the ASP Plateau, and at 88°E, 97°E, and 111°E (at along-axis distances from St. Paul island of 910, 1800, and ~2850 km, respectively). The latter three peaks are located near the centers of regional segmentation of the ridge defined by the persistence of fracture zone anomalies in satellite gravity data. This zeroth-order segmentation is comprised of several coherent tectonic units, up to ~900 km in length along-axis, that have been stable since reorientation of the SEIR when it migrated over the Kerguelen mantle plume at 38 Ma [*Small et al*., 1999]. *Graham et al*. [2001] used a spatial correlogram analysis to evaluate the length scales of helium isotope variability along the SEIR. The correlogram revealed crude structures in the He isotope variations at ~150 and ~400 km length scales which they interpreted to relate to upper mantle heterogeneity and secondary convection scales. The new, dense sampling for the current study by the French GEISEIR expeditions (**GE**ochimie **I**sotopique de la **SEIR**) represents a suite of more closely spaced (5–10 km) basalt glasses that stretch over a distance of more than 1600 km. This sampling provides a unique opportunity to quantify $^3He/^4He$ variations at moderately high resolution, for more than 1500 km along this mid-ocean ridge spreading center where systematic geochemical variations are present.

2. Field Sampling and Analytical Methods

The GEISEIR I and II expeditions took place aboard the R/V Marion Dufresne, in austral summers of 2009 and 2010. GEISEIR I sampled the ridge axis between 88.5°E and 99.3°E (along-axis distance from St. Paul of 875–2010 km; Figure 1) at varying sample density. Between 88.5°E and 96°E the sampling density was

Table 1. $^{3}He/^{4}He$, He and CO_2 Concentrations for Indian Ocean MORB Glasses

Sample	Segment	Location	Longitude (°E)	Latitude (°S)	Depth (m)	Distance (km)	$^{3}He/^{4}He$ (R/R_A)	2-sigma (R/R_A)	Vesicle [He] (ccSTP/g)	Vesicle [CO_2] (ccSTP/g)
GSR2 WC A1-1	K	axis	80.975	41.105	2600	395.3	7.63	0.05	3.89E-06	3.53E-02
GSR2 WC A1-2	K	axis	81.069	41.170	2612	405.9	7.85	0.06	2.42E-06	1.87E-02
GSR2 WC A1-3	K	axis	81.238	41.299	2688	426.1	7.67	0.06	8.83E-06	1.13E-01
GSR2 WC A1-5	K	axis	81.373	41.463	2563	446.8	7.63	0.08	1.03E-06	6.99E-03
GSR2 WC A1-5/6	K	axis	81.471	41.538	2520	458.5	7.83	0.05	4.04E-06	2.41E-02
GSR2 WC A1-6	K	axis	81.583	41.587	2537	468.9	7.60	0.05	4.33E-06	4.55E-02
GSR2 WC A1-7	K	axis	81.662	41.660	2524	479.3	7.67	0.07	8.14E-06	7.74E-02
GSR2 WC A1-8	K	axis	81.777	41.745	2558	492.7	7.63	0.05	5.97E-06	6.51E-02
GSR2 WC A1-9c	K	axis	81.910	41.801	2690	505.0	7.64	0.06	2.34E-06	1.65E-02
GSR2 WC A1-10	K	axis	81.982	41.883	2763	515.6	7.59	0.06	1.22E-05	1.49E-01
GSR2 WC A1-11	K	axis	82.060	41.963	2716	526.4	7.60	0.06	2.46E-06	9.03E-02
GSR2 WC A1-12b	K	axis	82.152	42.050	2510	538.6	7.75	0.11	5.28E-07	1.79E-04
GSR2 WC A1-13b	K	axis	82.221	42.114	2473	547.6	7.61	0.09	8.26E-07	5.89E-03
GSR2 WC A1-14	K	axis	82.317	42.172	2620	557.7	7.61	0.06	2.30E-06	1.74E-02
GSR2 WC A1-15	K	axis	82.397	42.242	2769	567.8	7.56	0.06	3.00E-06	2.29E-02
GSR2 WC A1-16	K	axis	82.485	42.304	2735	577.9	7.53	0.07	6.34E-06	4.30E-02
GSR2 WC A1-16/17	K	axis	82.563	42.366	2705	587.3	8.07	0.06	1.20E-05	5.17E-02
GSR2 WC A1-17	K	axis	82.623	42.427	2577	595.5	7.92	0.05	4.87E-06	1.14E-02
GSR2 WC A1-18	K	axis	82.713	42.492	2540	605.7	8.39	0.06	2.46E-06	2.76E-02
GSR2 WC A1-19	K	axis	82.827	42.538	2575	616.1	8.24	0.08	1.13E-06	6.95E-03
GSR2 WC A1-20	K	axis	82.932	42.593	2616	626.6	8.05	0.07	7.16E-06	4.97E-02
GSR2 WC A1-21	K	axis	83.037	42.660	2635	637.9	7.96	0.05	6.08E-06	5.80E-02
GSR2 WC A1-22	K	axis	83.123	42.729	2680	648.3	7.77	0.06	2.35E-06	8.83E-02
GSR2 WC A1-23	K	axis	83.203	42.790	2812	657.7	7.92	0.07	6.80E-06	3.47E-02
GSR1 WC-A2	L	axis	87.724	41.893	2427	874.5	9.41	0.06	1.33E-05	1.01E-01
GSR2 WC A2-1	L	axis	87.977	42.057	2363	902.1	9.51	0.07	1.05E-05	6.13E-02
GSR2 WC A2-2	L	axis	87.881	42.005	2398	892.3	9.38	0.07	8.71E-06	1.61E-02
GSR2 WC A2-3	L	axis	87.801	41.951	2434	883.4	9.30	0.06	1.33E-05	9.63E-02
GSR2 WC A2-4	L	axis	87.627	41.833	2453	864.0	10.05	0.07	9.44E-06	nd
GSR2 WC A2-4 replicate	L	axis	87.627	41.833	2453	864.0	10.04	0.07	9.82E-06	1.78E-02
GSR2 WC A2-5	L	axis	87.530	41.773	2455	853.6	9.60	0.06	1.79E-05	9.47E-02
GSR2 WC A2-6	L	axis	87.438	41.713	2442	843.4	9.51	0.05	1.82E-05	1.09E-01
GSR2 WC A2-7	L	axis	87.348	41.650	2439	833.2	9.65	0.07	1.13E-05	5.56E-02
GSR2 WC A2-8	L	axis	87.262	41.588	2458	823.3	9.52	0.06	1.07E-05	6.00E-02
GSR2 WC A2-9	L	axis	87.163	41.531	2385	812.9	8.92	0.06	1.16E-05	7.22E-02
GSR2 WC A2-10	L	axis	87.033	41.553	2280	806.1	8.53	0.05	5.71E-06	3.89E-02
GSR2 WC A2-11	L	axis	86.938	41.494	2359	795.8	8.39	0.07	8.34E-06	6.78E-02
GSR2 WC A2-12	L	axis	86.847	41.430	2296	785.5	8.72	0.06	1.03E-05	7.36E-02
GSR2 WC A2-13	L	axis	86.756	41.366	2356	775.1	8.72	0.06	1.80E-05	1.53E-01
GSR2 WC A2-14	L	axis	86.636	41.366	2506	767.3	8.65	0.05	4.59E-06	2.39E-02
GSR2 WC A2-15	L	axis	86.531	41.313	2493	756.9	8.63	0.06	1.72E-05	5.37E-02
GSR2 WC A2-16	L	axis	86.439	41.254	2498	746.8	8.73	0.06	3.39E-06	7.33E-02
GSR2 WC A2-17	L	axis	86.339	41.192	2547	735.9	8.58	0.06	1.34E-05	8.51E-02
GSR2 WC A2-18	L	axis	86.243	41.137	2585	725.9	8.24	0.05	5.82E-06	3.97E-02
GSR2 WC A2-19	L	axis	86.155	41.072	2648	715.5	8.64	0.06	1.70E-05	1.20E-01
GSR2 WC A2-20	L	axis	86.061	41.013	2743	705.3	8.56	0.06	3.96E-06	2.04E-02
GSR1 WC B7	C17	axis	88.699	41.704	2620	924.9	9.40	0.07	1.11E-05	7.44E-02
GSR1 DR B4-1	C17	axis	88.835	41.803	2560	940.6	9.51	0.09	1.05E-06	5.60E-04
GSR1 WC B5	C17	axis	89.057	41.921	2392	963.1	9.48	0.06	1.64E-05	1.37E-01
GSR1 DR B3-1(interior glass)	C17	axis	89.153	41.960	2243	972.1	7.63	0.06	4.30E-06	2.66E-02
GSR1 DR B3-1 (interior-repicatel)	C17	axis	89.153	41.960	2243	972.1	7.66	0.06	1.24E-05	1.03E-01
GSR1 DR B3-1(exterior glass)	C17	axis	89.153	41.960	2243	972.1	7.64	0.06	9.74E-06	7.44E-02
GSR1 DR B3-5	C17	axis	89.153	41.960	2243	972.1	7.66	0.07	7.94E-06	5.51E-02
GSR1 WC B2	C17	axis	89.412	42.169	2350	1003.1	8.92	0.06	2.50E-06	1.74E-02
GSR1 DR B2-9	C17	axis	89.540	42.230	2400	1015.6	9.52	0.06	7.75E-06	4.29E-02
GSR1 DR B1-14	C17	axis	89.694	42.327	2350	1032.3	8.43	0.13	5.07E-07	8.42E-04
GSR1 WC B21	C17	axis	89.797	42.360	2531	1041.2	8.68	0.06	1.39E-05	6.66E-02
GSR1 WC B20	C17	axis	89.878	42.421	2486	1050.6	8.65	0.07	2.64E-06	1.98E-02
GSR1 WC B19b	C16	axis	89.977	42.482	2505	1061.1	8.46	0.12	4.28E-07	1.53E-03
GSR1 DR B8-1	C16	axis	90.172	42.560	2790	1079.0	8.81	0.06	5.07E-06	5.13E-02
GSR1 WC B18	C16	axis	90.242	42.581	2530	1085.1	8.43	0.06	2.64E-06	1.99E-02
GSR1 DR B7-2 (exterior glass)	C16	axis	90.335	42.652	2530	1095.9	8.53	0.06	1.78E-05	1.76E-01
GSR1 WC B16	C16	axis	90.512	42.758	2672	1114.6	8.30	0.21	1.37E-07	6.60E-04
GSR1 WC B15b	C16	axis	90.595	42.784	2430	1121.7	8.33	0.07	1.43E-06	1.33E-02
GSR1 WC B14	C16	axis	90.677	42.828	2380	1130.0	8.52	0.06	3.48E-06	3.78E-02
GSR1 WC B13	C16	axis	90.843	42.927	2255	1147.4	8.20	0.06	7.32E-06	7.41E-02
GSR1 DR B6-2	C16	axis	90.953	42.984	2360	1158.4	8.41	0.07	6.56E-06	4.72E-02

Table 1. (continued)

Sample	Segment	Location	Longitude (°E)	Latitude (°S)	Depth (m)	Distance (km)	$^3He/^4He$ (R/R_A)	2-sigma (R/R_A)	Vesicle [He] (ccSTP/g)	Vesicle [CO_2] (ccSTP/g)
GSR1 WC B12	C16	axis	91.034	43.038	2380	1167.2	8.32	0.05	4.72E-06	4.43E-02
GSR1 WC B8	C16	axis	91.401	43.272	2790	1206.5	8.19	0.08	1.15E-06	7.69E-03
GSR1 DR B5-1	C16	axis	91.503	43.337	2670	1217.5	8.53	0.06	1.15E-05	7.82E-02
GSR1 DR B11-2	C16	axis	91.858	43.450	2737	1248.1	8.36	0.07	7.84E-06	6.30E-02
GSR1 WC B36	C16	axis	91.941	43.503	2910	1257.0	8.33	0.17	3.11E-07	3.26E-03
GSR1 DR B10-2	C15	axis	92.228	43.347	2400	1265.8	8.52	0.06	2.55E-06	2.40E-02
GSR1 WC B33	C15	axis	92.306	43.386	2583	1273.4	8.43	0.07	8.94E-06	1.03E-01
GSR1 WC B32	C15	axis	92.398	43.438	2557	1282.8	8.51	0.06	1.16E-05	1.31E-01
GSR1 WC B30	C15	axis	92.630	43.557	2540	1305.7	8.37	0.06	1.17E-05	9.78E-02
GSR1 WC B29	C15	axis	92.764	43.633	2558	1319.4	8.62	0.05	4.08E-06	7.50E-03
GSR1 WC B28	C15	axis	92.845	43.692	2484	1328.5	8.64	0.06	1.27E-05	7.29E-02
GSR1 WC B27	C15	axis	92.933	43.743	2509	1337.6	8.49	0.06	1.07E-05	4.56E-02
GSR1 DR B9-1	C15	axis	93.017	43.796	2580	1346.4	8.53	0.07	8.12E-06	8.66E-02
GSR1 WC B26b	C15	axis	93.086	43.828	2531	1353.0	8.49	0.07	2.52E-06	2.17E-02
GSR1 WC B25	C15	axis	93.234	43.897	2673	1367.1	8.52	0.05	4.94E-06	5.05E-02
GSR1 WC B24b	C15	axis	93.355	43.922	2634	1376.6	8.01	0.06	3.97E-06	3.09E-02
GSR1 WC B23	C15	axis	93.456	43.980	2657	1387.0	8.00	0.07	1.93E-06	1.49E-02
GSR1 WC B22	C15	axis	93.547	44.023	2721	1395.7	8.10	0.07	7.01E-06	3.88E-02
GSR1 DR B12-1	C15	axis	93.648	44.078	2703	1405.8	7.97	0.07	5.91E-06	5.27E-02
GSR1 WC B52	C15	axis	93.853	44.158	2906	1424.3	8.18	0.07	1.80E-06	8.70E-03
GSR1 DR B15-2	C15	axis	93.940	44.188	2800	1431.9	8.43	0.06	2.29E-06	1.48E-02
GSR1 WC B51	C15	axis	94.032	44.231	2926	1440.6	8.10	0.05	5.08E-06	3.86E-02
GSR1 DR B14-1	C15	axis	94.149	44.274	2820	1451.0	8.23	0.06	2.31E-06	1.81E-02
GSR1 WC B49b	C15	axis	94.310	44.413	3042	1470.3	8.15	0.05	5.30E-06	4.00E-02
GSR1 WC B47	C14	axis	94.336	44.569	2817	1481.7	7.75	0.05	3.30E-06	4.22E-03
GSR1 DR B13-2	C14	axis	94.426	44.600	2760	1489.5	7.68	0.05	3.86E-06	3.65E-02
GSR1 WC B45	C14	axis	94.604	44.724	2696	1508.9	7.78	0.07	7.56E-06	3.48E-02
GSR1 WC B44b	C14	axis	94.680	44.762	2667	1516.2	7.73	0.06	9.06E-06	6.49E-02
GSR1 WC B43b	C14	axis	94.769	44.805	2694	1524.6	7.86	0.06	9.51E-06	6.84E-02
GSR1 WC B42	C14	axis	94.925	44.884	2779	1539.8	7.80	0.07	1.72E-06	1.33E-02
GSR1 WC B41	C14	axis	95.010	44.923	2919	1547.8	7.84	0.06	8.62E-06	7.89E-02
GSR1 WC B40	C14	axis	95.088	44.957	2727	1554.9	7.77	0.05	1.40E-05	1.04E-01
GSR1 WC B39	C14	axis	95.258	45.043	2870	1571.3	7.58	0.05	5.10E-06	5.68E-02
GSR1 WC B38	C14	axis	95.340	45.082	2960	1579.1	7.69	0.05	2.58E-06	2.67E-02
GSR1 WC B55	C14	axis	96.034	45.156	2674	1629.3	8.18	0.06	1.17E-05	6.16E-02
GSR1 WC B54	C14	axis	96.217	45.250	2772	1646.9	8.09	0.05	1.01E-05	1.05E-01
GSR1 WC B53	C14	axis	96.313	45.303	2825	1656.5	8.08	0.07	2.06E-06	1.49E-02
GSR1 DR C8-1	C13/14	Smt	96.120	45.833	2000	1675.5	7.88	0.18	2.22E-07	3.67E-04
GSR1 DR C7-3	C13/14	Smt	95.867	46.215	1460	1682.1	7.98	0.06	2.40E-06	7.50E-03
GSR1 DR C6-2	C13/14	axis	95.726	45.947	3500	1656.8	7.82	0.07	1.19E-06	8.13E-03
GSR1 WC C49	C13/14	axis	95.773	46.018	3137	1664.1	7.78	0.06	6.69E-06	5.73E-02
GSR1 WC C48	C13/14	axis	95.831	46.047	3195	1669.6	7.90	0.06	1.14E-05	8.10E-02
GSR1 DR C5-12	C13/14	axis	95.932	46.088	2994	1678.7	7.35	0.06	1.92E-06	1.56E-02
GSR1 WC C46	C13/14	axis	96.112	46.217	3110	1698.1	7.83	0.06	8.82E-06	6.63E-02
GSR1 WC C45	C13/14	axis	96.189	46.257	3206	1705.4	7.75	0.05	3.70E-06	3.52E-02
GSR1 WC C43	C13	axis	96.059	46.624	2517	1719.3	8.50	0.08	1.39E-06	6.85E-03
GSR1 WC C42	C13	axis	96.117	46.656	2517	1724.9	7.86	0.06	8.51E-06	1.01E-01
GSR1 WC C38	C13	axis	96.298	46.746	2465	1741.8	8.48	0.07	7.00E-06	3.83E-02
GSR1 WC C36	C13	axis	96.451	46.834	2583	1756.9	8.34	0.05	5.61E-06	4.08E-02
GSR1 WC C35	C13	axis	96.512	46.872	2511	1763.1	8.32	0.14	3.50E-07	4.89E-04
GSR1 WC C34	C13	axis	96.571	46.896	2556	1768.3	8.19	0.05	1.29E-05	1.07E-01
GSR1 WC C33	C13	axis	96.627	46.925	2580	1773.6	8.37	0.05	1.45E-05	1.02E-01
GSR1 DR C4-1	C13	axis	96.692	46.952	2620	1779.4	8.27	0.05	5.85E-06	5.74E-02
GSR1 WC C31	C13	axis	96.764	47.053	2576	1790.1	8.70	0.06	1.00E-05	9.89E-02
GSR1 WC-C30	C13	axis	96.896	47.120	2597	1802.4	8.39	0.06	9.84E-06	8.10E-02
GSR1 WC C29	C13	axis	96.948	47.160	2603	1808.1	8.31	0.05	3.99E-06	2.63E-02
GSR1 WC C28	C13	axis	97.009	47.191	2591	1813.9	8.35	0.05	1.73E-05	1.44E-01
GSR1 WC C27	C13	axis	97.089	47.210	2578	1820.1	8.52	0.06	3.28E-06	2.22E-02
GSR1 WC C26	C13	axis	97.160	47.242	2530	1826.5	8.31	0.05	1.16E-05	1.05E-01
GSR1 WC C25	C13	axis	97.225	47.268	2545	1832.3	7.96	0.06	1.04E-05	1.01E-01
GSR1 WC C24	C13	axis	97.262	47.315	2517	1837.4	8.16	0.07	6.33E-06	4.20E-02
GSR1 WC C23	C13	axis	97.319	47.356	2448	1843.4	8.20	0.06	8.82E-06	6.07E-02
GSR1 WC C22	C13	axis	97.378	47.385	2413	1848.9	8.11	0.06	8.34E-06	7.92E-02
GSR1 WC C20	C13	axis	97.554	47.476	2434	1865.5	7.88	0.06	1.15E-05	9.36E-02
GSR1 WC C19b	C13	axis	97.603	47.500	2435	1870.0	7.91	0.05	4.14E-06	3.56E-02
GSR1 WC C18	C13	axis	97.677	47.533	2477	1876.7	7.61	0.04	6.78E-06	4.34E-02
GSR1 WC C17	C13	axis	97.740	47.569	2487	1882.8	7.70	0.05	1.34E-05	6.33E-02

Table 1. (continued)

Sample	Segment	Location	Longitude (°E)	Latitude (°S)	Depth (m)	Distance (km)	$^3He/^4He$ (R/R_A)	2-sigma (R/R_A)	Vesicle [He] (ccSTP/g)	Vesicle [CO_2] (ccSTP/g)
GSR1 WC 15b	C13	axis	97.862	47.623	2537	1893.7	8.01	0.05	3.84E-06	2.02E-02
GSR1 WC C13b	C13	axis	97.995	47.656	2696	1904.1	7.80	0.05	4.96E-06	4.47E-02
GSR1 WC C11b	C13	axis	98.094	47.697	2778	1912.8	7.85	0.05	1.50E-05	1.47E-01
GSR1 WC C9	C13	axis	98.237	47.790	2700	1927.3	7.86	0.05	1.42E-05	1.25E-01
GSR1 DR C3-4	C13	axis	98.415	47.832	2607	1941.1	7.84	0.08	9.54E-07	6.45E-02
GSR1 WC C7b	C13	axis	98.453	47.880	2741	1946.3	7.80	0.05	3.98E-06	4.74E-02
GSR1 DR C2-2	C13	axis	98.545	47.897	2640	1953.1	7.98	0.05	1.80E-05	1.25E-01
GSR1 WC C4	C13	axis	98.770	47.978	2830	1972.2	7.86	0.06	1.03E-05	1.13E-01
GSR1 WC C2b	C13	axis	99.035	48.116	2811	1996.9	7.77	0.05	1.29E-05	1.41E-01
GSR1 DR C1-1	C13	axis	99.174	48.133	2730	2006.7	7.82	0.09	7.83E-07	5.93E-03
SEIR-WW10 Samples										
WW10 66-9	C17	Smt	89.313	41.713	1375	965.9	10.22	0.08	1.48E-06	2.40E-04
WW10 67-13	C17	Smt	89.183	41.878	1850	968.5	9.70	0.06	5.77E-06	2.62E-02
WW10 72-2	C16	Smt	91.283	43.417	1470	1208.3	8.34	0.09	8.68E-07	4.21E-04
WW10 79-19	C14	axis	95.409	45.106	3020	1585.1	7.66	0.07	1.82E-06	1.78E-02
WW10 83-17	C14	axis	95.764	45.051	3069	1605.1	8.00	0.24	4.06E-08	4.21E-04
WW10 85-19	C13/14	axis	96.127	45.195	2555	1637.7	8.12	0.07	2.51E-06	2.38E-02
WW10 88-1	C13	axis	96.833	47.076	2568	1795.8	9.46	0.05	7.34E-06	4.10E-02
WW10 105-1	C11	axis	103.038	47.765	2783	2238.1	7.30	0.04	3.53E-06	2.77E-02
WW10 132-1	C5	axis	111.783	50.212	3328	2930.6	7.23	0.06	9.26E-07	4.11E-03
SWIR										
MD34-7		axis	36.30	44.81	1500		7.59	0.06	nd	nd
MD34-6		axis	38.80	44.18	2190		8.47	0.06	nd	nd
MD34-5		axis	40.65	43.89	2550		7.00	0.05	nd	nd
MD34-4		axis	43.70	40.98	3700		7.68	0.06	nd	nd
MD34-3		axis	49.88	37.71	3260		9.62	0.07	nd	nd
MD34-2		axis	56.27	33.76	3800		9.10	0.06	nd	nd
MD34-1		axis	57.84	31.69	4050		8.49	0.06	nd	nd
Agulhas 53-1-32		axis	32.67	47.17	3250		8.05	0.04	6.94E-07	nd
Agulhas 53-3-3		axis	34.07	46.03	3250		8.48	0.04	7.97E-07	nd
Protea5 D37-2		axis	45.77	40.13	3075		7.15	0.04	2.86E-07	nd

~0.1 km^{-1} (1 sample per 10 km), and between 96°E and 99.3°E it was 0.2 km^{-1} (1 sample per 5 km). GEISEIR II sampled the ridge axis between 81°E and 88°E at sampling density of ~0.1 km^{-1}. Recovery was extremely good at >150 sites using the newly designed French wax corer (nicknamed Hellboy) supplemented with ~30 dredge localities. For example, along the midsection of the 96°E–99°E sampling, recovery was typically 50–100 g of extremely fresh glass at every locality and sample appearance suggests that this section of the ridge is currently active or has been active very recently.

Large, fresh glass chunks from the wax core and dredge collection were first cleaned ultrasonically in ethanol and acetone, followed by drying in air. Pieces free of surface alteration and obvious cracks were handpicked under a binocular microscope. Helium isotope analyses were carried out by crushing in vacuum, liberating helium and associated gases (primarily CO_2) from vesicles trapped within the glass. Typically 200–300 mg of fresh glass (several mm-sized chips) were loaded into stainless steel crushers between a thin, removable stainless steel disk anvil at the tube bottom and an overlying magnetic piston. The magnetic piston was lifted using a system of external solenoids and actively forced onto the sample 75 times to produce high impact strokes. The sample was crushed to a powder while still connected to the vacuum line. The released CO_2 and any minor H_2O were condensed together during the crushing at 77 K (liquid N_2 temperature) in a stainless U-tube section. Noncondensable reactive gases were removed using SAES® Zr-Al getters. Noble gases were separated onto a cryogenically controlled charcoal trap at 10 K. The trap was warmed to 45 K and helium was admitted directly to the mass spectrometer for isotope ratio and peak height determination, while Ne and other noble gases were held behind. Line blanks were always performed before sample analysis and were typically $<5 \times 10^{-11}$ cm^3 STP ^4He.

Helium isotope analyses were performed using a Nu Instruments® noble gas mass spectrometer at Oregon State University (OSU). Helium concentrations were determined by peak height comparison to standards, and CO_2 concentrations were determined by capacitance manometry following distillation of CO_2 from H_2O

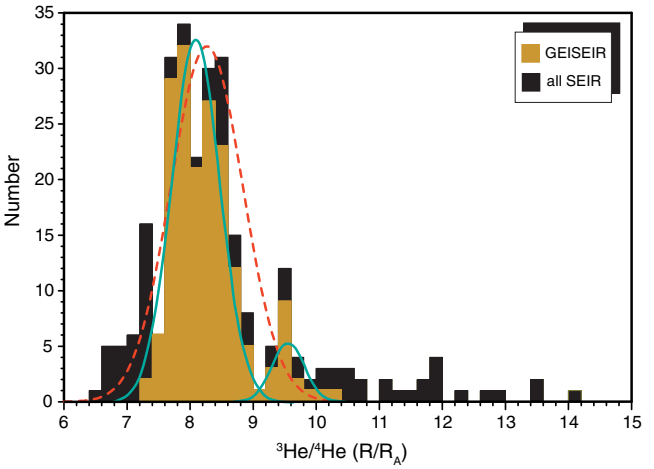

Figure 3. Histogram of ^{3}He/^{4}He for Southeast Indian Ridge basalts. Replicate analyses have been averaged. The dashed red curve depicts a unimodal Gaussian distribution for the densely sampled region between 81°E and 100°E (segments K, L, and C13–C17. Range = 7.18–10.22; Mean = 8.24, s.d. = 0.58, skewness = 1.04, median = 8.18; n = 175 sample locations). The solid blue curves depict a mixing analysis describing the histogram as a bimodal distribution, where one subpopulation has mean ^{3}He/^{4}He = 8.12 R$_A$ ± 0.37 (1 s.d.) and a proportion of 0.90, while the other subpopulation has mean ^{3}He/^{4}He = 9.57 R$_A$ ± 0.26 and a proportion of 0.10.

into a calibrated volume of the sample extraction line using liquid nitrogen and frozen isopropanol traps. The mass spectrometer is fitted with a high-sensitivity ion source (Nier-type) and is operated under static vacuum. It is all-metal construction and can be baked to reach low background levels and low static gas rise rates. The instrument is fitted with a single faraday cup and three ion-counting detectors. The high mass ion counter position is shared with the faraday with switching via an electrostatic deflector. The central and low mass ion-counting detectors have a special filter to eliminate scattered low energy ions that may interfere with small ion beams (which can be especially important when trying to measure very small amounts of ^{3}He in the presence of large amounts of ^{4}He, for example). The OSU mass spectrometer is a variable dispersion instrument that employs specially designed electrostatic lenses. It performs the ^{3}He/^{4}He measurement in a pseudohigh-resolution mode that partially resolves ^{3}He from $HD^+ + H_3^+$. During the course of this study, on peak $HD^+ + H_3^+$ count rates were typically 25 cps during the course of the analysis. Beneath the peak-flat where ^{3}He was measured the $HD^+ + H_3^+$ count rate was effectively zero.

Gas standards to calibrate the instrument's sensitivity and mass discrimination include both marine air and a high ^{3}He/^{4}He gas standard (the helium standard of Japan, HESJ) [*Matsuda et al.*, 2002]. The HESJ used as a running standard during this study was subsampled from the same batch provided to the National Oceanic and Atmospheric Administration/Pacific Marine Environmental Laboratory [*Lupton and Evans*, 2004]. It was calibrated with the OSU noble gas mass spectrometer against marine air collected in 2007 at the Oregon coast, and found to have ^{3}He/^{4}He (20.4 R$_A$) identical to the HESJ subsample routinely used at NOAA/PMEL.

Several samples have been analyzed in duplicate or triplicate during this study in order to assess sample reproducibility at OSU and to compare the results to earlier analyses [*Graham et al.*, 2001]. Two samples from the WW10 expedition (72-2 and 88-1) previously analyzed at NOAAA/PMEL were reanalyzed and the results agree within analytical uncertainty (8.34 ± 0.09 versus 8.21 ± 0.06 and 9.46 ± 0.05 versus 9.38 ± 0.05, respectively). One of the newly collected basalts having elevated ^{3}He/^{4}He (GSR II A2-4) was analyzed twice in the OSU lab and the results agree within uncertainty (10.04 and 10.05 R$_A$). Another sample (GSR I DR B3-1 from segment C17), in which the interior and exterior portions of thick glass from a single basalt could be separated, was analyzed three times and each time gave the same isotopic result (7.63, 7.66, and 7.64 R$_A$). Lastly, one sample (GSR I DR C5–12 from segment C13/14) was found to have a ^{3}He/^{4}He ratio (7.35 R$_A$) similar to that for a previously analyzed sample (WW10 WC48 with ^{3}He/^{4}He = 7.31 R$_A$) collected from the same location. This last comparison indicates that the low ^{3}He/^{4}He anomaly in the midsection of segment C13/14 is confined to a restricted area (<10 km length), similar to what is observed for sample DR B3-1 along segment C17.

3. Results

Results for vesicle ^{3}He/^{4}He, and He and CO_2 concentrations in the new sample suite are reported in Table 1. Table 1 also includes analyses of nine WW10 basalts from the SEIR to supplement the new GEISEIR results.

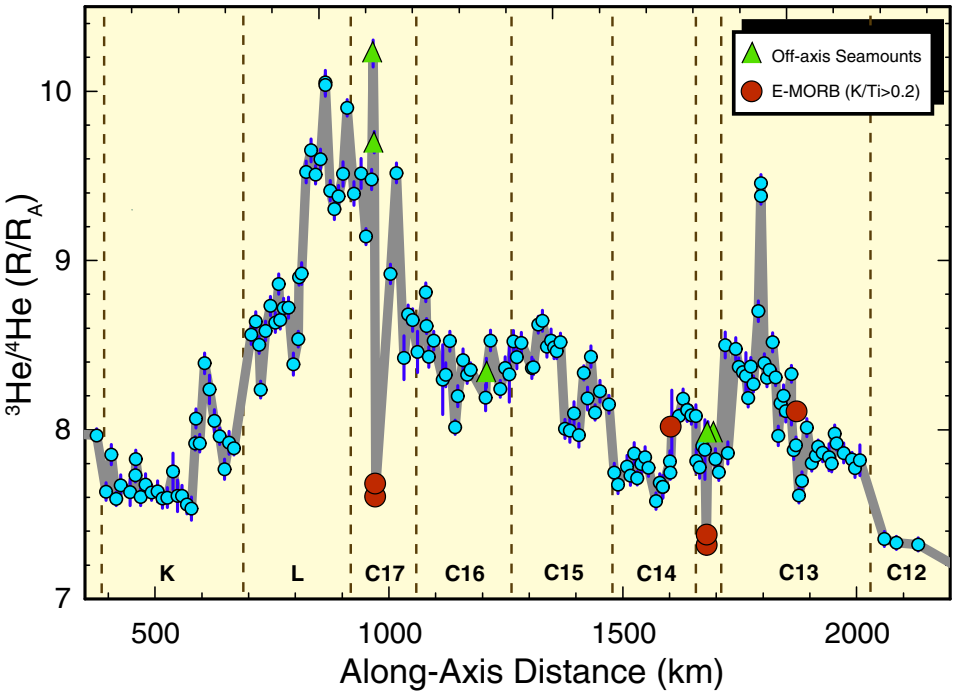

Figure 4. ^{3}He/^{4}He along the densely sampled portion of the SEIR axis between 81°E and 101°E (distance is shown in km from the location of St. Paul island). Vertical dashed lines delineate boundaries to the first-order and second-order tectonic segmentation of the ridge axis.

We also report data for 10 basalt glasses from the Southwest Indian Ridge (SWIR, from expeditions of Marion Dufresne 34, Agulhas 53, and Protea 5) for which Pb, Nd, Sr, and Hf isotope compositions have been previously published [*Hamelin and Allegre*, 1985; *Mahoney et al*., 1989, 1992; *Chauvel and Blichert-Toft*, 2001; *Janney et al*., 2005].

Vesicle He concentrations range between 0.2 and 18 μccSTP/g (Table 1), and values at the high and low ends of this concentration range occur thoughout the study area. There is no obvious covariation of ^{3}He/^{4}He with He concentration, MgO content or Fe/MgO ratio (not shown). Likewise there are no simple relationships in the overall data set, or in the data grouped by individual segments, between He concentration or He/CO_2 ratio and axial depth. The helium isotope variability in these SEIR basalt glasses is therefore not explained by shallow-level processes operating in the crust (e.g., radiogenic ingrowth of degassed magma during prolonged storage in the crust is insignificant in producing the observed ^{3}He/^{4}He variations).

A histogram of ^{3}He/^{4}He (Figure 3) compares the new results to the rest of the SEIR. The samples collected between 81°E and 100°E (n = 175) show a ^{3}He/^{4}He range of 7.2–10.2 R_A, which is more than half the range in MORB glasses (~6–11 R_A) erupted away from the influence of ocean island hot spots having high ^{3}He/^{4}He [*Graham*, 2002; *Kurz et al*., 2005]. ^{3}He/^{4}He ratios for samples between 81°E and 100°E have an approximate Gaussian distribution. Its median is 8.17 R_A, identical to the value of 8.1 R_A previously computed for MORBs from each of the Atlantic, Indian, and Pacific Ocean basins [*Graham*, 2002]. In detail, there may be a slightly increased proportion of ^{3}He/^{4}He values above 9 R_A (10% of the samples analyzed) compared to what is expected for a single Gaussian population. A mixture analysis of the new ^{3}He/^{4}He data shows that when it is deconvolved into two distinct normal populations, population 1 has mean ^{3}He/^{4}He = 8.12 R_A ± 0.37 (1 s.d.) and a proportion of 0.90, while population 2 has mean ^{3}He/^{4}He = 9.57 R_A ± 0.26 and a proportion of 0.10 (Figure 3). This possible bimodality has implications for estimating the upper limit of ^{3}He/^{4}He in depleted upper mantle away from high-^{3}He/^{4}He hot spots, and where recyled low-^{3}He/^{4}He material is absent (discussed further below).

^{3}He/^{4}He variations are evident at a variety of length scales (Figure 4), ranging from long (~1000 km), to intermediate (~100 km) and to short (~20–40 km) distances. Numerous examples of abrupt, along-axis transitions in ^{3}He/^{4}He can be found. Some of these abrupt changes occur near tectonic segment

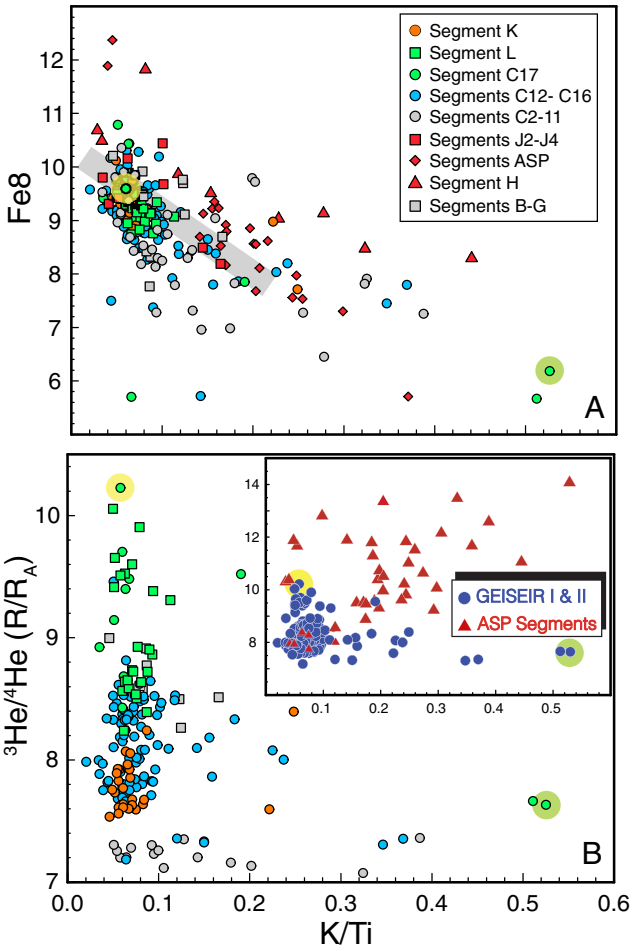

Figure 5. (a) Fe_8 and (b) $^3He/^4He$ (R/R_A) versus K/Ti (elemental weight ratio) for SEIR basalts. Data are from this study plus *Douglas Priebe* [1998], *Graham et al.* [1999, 2001], *Johnson et al.* [2000], and *Nicolaysen et al.* [2007]. The two highlighted samples are the enriched basalt GSR I DR-B3-1 (green) and the depleted basalt WW10 66-9 (yellow) from segment C17 that are separated by <10 km. For reference, the gray line depicts the linear regression for regional averages of the global MORB data set from *Shen and Forsyth* [1995].

boundaries (e.g., K/L, C15/14, C13/12). However, there are clear examples of abrupt changes not associated with such boundaries that sometimes occur in the middle of a segment (e.g., L, C15, C14, C13).

Abrupt excursions to low $^3He/^4He$ ($\leq$7.65 R_A) ratios are notable in four particular E-MORB glasses. E-MORBs are defined here as having an elemental K/Ti ratio >0.2. The notable cases are samples DR B3-1 (analyzed in triplicate) and B3-5 along segment C17, and samples DR C5-12 and WW10 WC48 from the same area in the middle of the short segment C13/14. These E-MORBs occur as isolated examples far from ridge segment boundaries. Seamounts are present both north and south of segment C13/14 at the same longitude as the central portion where its E-MORBs were recovered. Each of those seamounts (samples DR C7-3 and C8-1) erupted low-K/Ti basalts that have higher $^3He/^4He$ ratios than the E-MORBs, and are similar to the depleted MORBs recovered elsewhere along C13/C14. This further confirms that the low-$^3He/^4He$ signature along C13/14 is restricted to a small area (<10 km).

The low $^3He/^4He$ in the E-MORBs from segments C17 and C13/14 (Figure 4) are also the lowest ratios found for hundreds of kilometers along the SEIR. The value of 7.5 R_A along C17 corresponds precisely to the low (and uniform) values observed along segments K and much of C14, each of which is ~400–500 km away. The E-MORB signature along C13/14 has a slightly lower $^3He/^4He$ than along C17, and it resembles the low values observed to its east along C12 which is also ~400 km away. While segments K and C12 show relatively low and uniform $^3He/^4He$ they do not typically erupt E-MORBs. This pattern of occurrence suggests that enriched mantle heterogeneities may be widespread in the subridge mantle, but only occasionally do they give rise to E-MORB chemical compositions. In contrast, the presence of enriched heterogeneities may be the primary cause of downward variations in $^3He/^4He$, from typical ambient values of 8.5 R_A or higher.

Abrupt excursions to high $^3He/^4He$ also occur throughout the study area. Notably, along segment C13 where our sampling density is the highest (1 sample per 7 km of ridge), $^3He/^4He$ increases abruptly to 9.4 R_A (in sample WW10 88-1) from background values of 8.2 to 8.4 R_A that extend over >100 km of this ridge segment This abrupt change occurs over 15 km or less. Similarly, the region of broadly elevated $^3He/^4He$ along the eastern portion of segment L and the western portion of segment C17 shows $^3He/^4He$ spike-like increases (up to 10 R_A in sample GSR II WC A2–4). These spikes occur over distances of ~10 km or less.

The highest $^3He/^4He$ ratios in the 81°E–100°E region are generally found in depleted basalt glasses characterized by low K/Ti (Figure 5b). This contrasts markedly with the basalts from the Amsterdam-St. Paul

vicinity, where $^3He/^4He$ and K/Ti show a generally positive relationship due to the enriched hot spot effect on depleted mantle beneath the ridge axis (Figures 2 and 5b). Between 81°E and 100°E, highly depleted lavas occur along the ridge axis and also just outside the axial region. The highest $^3He/^4He$ occurs in a low-K/Ti basalt (WW10 66-9) recovered from ~1375 m water depth near the summit of a large seamount immediately north of the spreading ridge at 89.3°E (Figure 5). The high $^3He/^4He$ in this seamount basalt also occurs within 10 km of the E-MORBs along segment C17 that have distinctly low $^3He/^4He$ (DR C3-1 and C3-5).

In contrast to the above examples of significant $^3He/^4He$ variability over short length scales in the study area, there are also examples where large sections of the ridge axis have uniform $^3He/^4He$. The best case is the ~180 km section of segment K (between 395 and 578 km distance from St. Paul). Here the total $^3He/^4He$ range (for 18 samples collected at approximately 10 km intervals) is 7.53–7.85 R_A, and 16 of the samples lie between 7.53 and 7.75 R_A. The mean and standard deviation for this section of the SEIR are 7.65 ± 0.086 R_A, which corresponds to a total variability of ±1.1%. This is similar to the variability observed in the Lucky Strike area of the Mid-Atlantic Ridge [*Moreira et al*., 2011], which is currently the most densely sampled portion of the mid-ocean ridge system for $^3He/^4He$. Although the ridge length covered by that study was very short (~13 km) the sampling density was very high (25 samples corresponding to a mean sample spacing of ~0.5 km) and $^3He/^4He$ averaged 8.28 ± 0.07 R_A (±0.9%). *Moreira et al*. [2011] attributed the uniformity in $^3He/^4He$ to lava eruptions from a well-mixed crustal magma lens. The limited variability observed here along much of segment K is comparable to that observed by *Moreira et al*. [2011], making our new results remarkable because they represent an order of magnitude increase in ridge length compared to Lucky Strike and these SEIR lavas are unlikely to be derived from a common magmatic system.

4. Discussion

4.1. Melting of Lithologically Heterogeneous Mantle and $^3He/^4He$ in SEIR Basalts

Previous studies along the SEIR have inferred that the He, Pb, Sr, Nd, and Th isotope variations are controlled by variations in the depth and extent of melting of heterogeneous mantle [*Graham et al*., 2001; *Mahoney et al*., 2002; *Nicolaysen et al*., 2007; *Russo et al*., 2009]. The melting process was thought to sample lithologically heterogeneous mantle in response to a lateral temperature gradient, extending from hotter mantle near the ASP Plateau to colder mantle beneath the Australian-Antarctic Discordance. U-series disequilibria in the SEIR basalts further revealed the connection between melting rate (which is strongly controlled by the lithologic constitution of the mantle), the extent of melting, mantle porosity, and the depth at which melting initiates [*Russo et al*., 2009]. However, there are no simple correlations between indicators of degree of melting (such as Na_8) and K/Ti in SEIR basalts, indicating that the K/Ti variability largely represents compositional heterogeneity in the mantle source region. Nor are there any simple correlations between K/Ti and Pb isotope ratios or ε_{Hf}, suggesting that each subpopulation that is distinguishable in terms of Pb and Hf isotope compositions involves derivation from both N-MORB and E-MORB mantle sources [*Hanan et al*., 2013].

In terms of $^3He/^4He$, however, we noted earlier that a mixture analysis of the $^3He/^4He$ histogram for the 81°E–101°E region could be deconvolved into two distinct subpopulations having $^3He/^4He = 8.1 \pm 0.8$ (2σ) R_A and $^3He/^4He = 9.6$ R_A ±0.6 (2σ) R_A (Figure 3). The relationship between $^3He/^4He$ and K/Ti also bears on this observation. Low $^3He/^4He$ occurs in SEIR basalts over the full range of K/Ti (Figure 5). However, all E-MORBs having K/Ti > 0.3 have low $^3He/^4He$ ratios (segments C17 and C13/14, plus two samples west of the study region toward the AAD). In contrast, the highest $^3He/^4He$ ratios (>9 R_A) typically occur in the most depleted lavas (15 of 17 samples have K/Ti < 0.1), and the highest ratio (10.2 R_A) is found in a depleted lava (K/Ti ~ 0.05) from the seamount immediately adjacent to the C17 ridge axis (Figure 5). Notably, $^3He/^4He$ ratios above 9 R_A are absent from E-MORBs altogether. As well, the negative $^3He/^4He$ – K/Ti correlation shows quite different behavior from that observed along the ASP-influenced section of the SEIR (Figure 5), where elevated $^3He/^4He$ (>14 R_A) is associated with higher K/Ti [*Graham et al*., 1999]. This different relationship between He isotopes and minor element variations for the ASP region versus the rest of the SEIR reinforces the notion that source heterogeneity, as revealed by variability in He isotopes, should be considered within the framework of lithologic variability (and its effect on partial melting), as revealed by variability in K/Ti.

It is well recognized that a small amount of garnet pyroxenite/eclogite embedded in peridotite may be responsible for a host of geochemical signatures in basalts. The landmark paper by *Hirschmann and Stolper*

[1996] paved the way to the idea that compositional variability in MORBs at short length scales can be related to the presence of small amounts of pyroxenite/eclogite within a mantle source comprised mostly of a peridotitic matrix. Pyroxenite has a lower solidus temperature, and primarily because it is pyroxene rich it has a higher melt productivity than peridotite. For example, the presence of ~5% pyroxenite could contribute as much as ~40% to the total melt of a peridotite-pyroxenite mixture. Unfortunately, the major element signature of pyroxenite in the ensuing basaltic melt is difficult to detect because it is similar in major element composition to a peridotite melt. In general, the melting of pyroxenite-peridotite mixtures in which the two components have different trace element and isotope compositions leads to a number of important complexities. Two of these are relevant to the present study; (1) the isotopic range observed in basalts is unlikely to represent the full range of heterogeneity in the mantle source region—i.e., the depleted peridotite composition may not be represented by even the most depleted MORB magma—and (2) isotope-isotope arrays do not necessarily point directly toward the mantle end-members [*Kellogg et al*., 2007; *Stracke and Bourdon*, 2009; *Rudge et al*., 2013].

Eclogite or garnet pyroxenite in the mantle may originate either as subducted ocean crust, delaminated lower continental crust, or trapped basaltic melt. Melts of these mafic lithologies alone typically have elevated FeO and no enrichment in K_2O [*Lambart et al*., 2013]. However, *Kogiso et al*. [1998] showed that melting a basalt-peridotite mixture may generate alkali-rich melts. Such mixtures can be formed by invasion of peridotite with partial melts derived from eclogite or by hybridization with peridotite as the recycled crust is thinned during convective stirring in the mantle. This yields olivine-bearing, silica-deficient pyroxenite [*Kogiso et al*., 2003] and changes the melting situation dramatically. Melts of such hybrid mantle will be alkalic and have low SiO_2 and CaO, and high Al_2O_3 and TiO_2. While the E-MORBs from segments C17 and C13/14 are not alkalic lavas, they do lie close to the alkaline/subalkaline boundary. Along with their elevated K_2O (0.7–1.2 wt %) and K/Ti and low $^3He/^4He$ (Figure 5), they have very low CaO/Al_2O_3 (0.60–0.65) at moderate values of MgO (~6.5–8.0 wt %). Because eclogite and garnet pyroxenite are olivine-free lithologies, primary magmas derived from them may have lower MgO than those derived from peridotite. The extent to which the crystallization of clinopyroxene at depth could be responsible for the lower CaO/Al_2O_3 traits requires a full assessment of the major element variations in the GEISEIR basalt glass suite and is beyond the scope of the present paper. We simply point out here that the E-MORB character of some of the lavas from the present study area appears to be consistent with the melting of a peridotite-eclogite mixture that may account for the low $^3He/^4He$ character.

There is a prevailing negative covariation of K/Ti with Fe_8 along the SEIR (Figure 5). This relationship is also observed in MORBs globally [*Shen and Forsyth*, 1995]. The observed negative covariation along the SEIR further supports the notion that the high-K/Ti mantle source is enriched in a "basaltic" component [*Langmuir and Hanson*, 1980]. This makes it difficult to know the extent to which one can attribute Fe_8 variations to changes in the initial depth of melting (or the mean depth of melting) as is commonly assumed. The broad covariation between $^3He/^4He$ and Fe_8 for the SEIR led *Graham et al*. [2001] to attribute the helium isotope variations to melting of heterogeneous mantle containing a small amount of garnet pyroxenite. Such lithologic heterogeneity should have lower $^3He/^4He$ if it originates from recycled crust or ancient trapped melt. Garnet pyroxenite or eclogite has a lower solidus temperature and will melt preferentially to surrounding mantle peridotite. It will also contribute a significantly smaller proportion to the total magma when melting begins at greater depth (at higher mantle temperature and pressure) because the pyroxenitic melts become increasingly diluted by partial melts of the peridotite at shallow depths. Following this reasoning, *Graham et al*. [2001] suggested that hotter mantle would begin to melt deeper, produce a shallower ridge axis, and produce melts having higher Fe_8 and $^3He/^4He$. This explanation implies that highly depleted (pyroxenite or eclogite free) regions of the upper mantle will have $^3He/^4He$ ratios of 9 R_A, or higher.

Russo et al. [2009] found that both N-type and E-type MORBs record a west-to-east decrease in ($^{230}Th/^{238}U$) activity ratio along the SEIR from 90°E to 118°E, with no systematic differences in Th-U disequilibria between the two MORB types. They carried out forward modeling of mixtures of melts derived from pyroxenite + peridotite to examine likely fractions of each melt type that would be consistent with the basalt observations. Using simple but reasonable assumptions, *Russo et al*. [2009] showed that garnet pyroxenite or eclogite comprises ~3–5% of the mantle beneath the easternmost SEIR, and lesser amounts in the 81°E and 100°E region. One possibility then is that the elevated $^3He/^4He$ ratios of 9–10 R_A along segments L and C17 approach the intrinsic He isotope composition for pyroxenite-free (harzburgite) upper mantle. It seems

doubtful though that melting of harzburgite alone would be sufficient to produce the shallower axial ridge in the 88°E region, as well as the relatively large seamounts immediately adjacent to the ridge (which rise to a water depth of ~1400 m).

The axial location of the E-MORBs is an additional observation that bears on any melting scenario for lithologically heterogeneous mantle. The two E-MORBs having the most extreme $^3He/^4He$ are the GSR I DR3 samples from segment C17, and the DR5 sample (plus WW10 WC48) from segment C13/14. Samples DR B3-1 and B3–5 were recovered from a small knob atop the axial volcanic ridge in segment C17; remarkably this locality corresponds to the shallowest depth of the axial ridge in the whole 81°E–100°E study area. In comparison, samples DR C5-12 and WW10 WC48 were recovered from the center of the small segment C13/14. This second example of low $^3He/^4He$ in E-MORBs also appears to be confined to a small and shallower section of the ridge axis. As noted earlier, seamounts are found just north and south of segment C13/14 at the same longitude as the central portion where the E-MORBs were recovered. Each of these seamounts (samples DR C7-3 and C8-1) erupted low K/Ti basalts that have $^3He/^4He$ ratios similar to other depleted MORBs from this area. The low $^3He/^4He$ signatures in the E-MORBs are, therefore, restricted to small areas (<10 km) in each case. These restricted occurrences along segments C17 and C13/14 imply that mantle heterogeneity is sampled almost exclusively by vertical melt transport beneath these areas of the ridge.

The presence of such enriched compositions at segment centers and shallow locations is not what would be expected from the *Klein and Langmuir* [1987] model of melt generation beneath ridges. That model predicts that the largest extents of melting and consequently the most depleted MORB magmas will be present beneath the shallowest sections of ridge. The nearby MORBs from segments C17 and C13/14 do have these requisite features. The rare occurrences of E-MORBs at the very shallowest locations suggest a linkage between melt generation from enriched mantle and rapid magma transport via formation of permeable conduits [*Katz and Weatherley*, 2012], and that this is sometimes more discernible beneath central axial highs. Perhaps the inward heat flux that drives the melting of the heterogeneity [*Katz and Rudge*, 2011] leads to a more discrete sampling of the enriched material when surrounding mantle regions have experienced extensive melting, thereby leading to E-MORB association with a local axial high. These E-MORB melts appear to have ascended from depth without significant interaction with the surrounding (and perhaps barren) peridotite or with depleted melts that may have been present in a magma lens. Elsewhere along the ridge, chemical evidence for the presence of enriched source material is more cryptic because the enriched melts become diluted en route with melts from surrounding peridotite. The presence of enriched heterogeneities appears to be responsible for much of the variability in basalt $^3He/^4He$, producing downward excursions from a background depleted peridotite value that is greater than 9 R_A beneath much of the SEIR.

4.2. Crustal Magma Lens Filtering of $^3He/^4He$ Variability

Magma redistribution complicates the simple mapping of surface variability in $^3He/^4He$ to mantle-scale variability. Both dike propagation within the crust and lateral mixing in crustal magma lenses or near the MOHO may be important. Along the fast-spreading East Pacific Rise (EPR), 5–15 km long crustal magma lenses are responsible for the fine-scale tectonic and geochemical segmentation [*Carbotte et al.*, 2013]. Upper crustal accretionary units at this scale along the EPR have distinct geochemical and morphological characteristics that reflect near vertical transport from the underlying magma lens. Our sampling interval in the GEISEIR study area (Figure 1) ranges from ~10 km in the west (along segments K, L, and C17 to C13/14) to ~5 km in the east (along segment C13). To a first order, this sampling density allows for tests of possible along-axis crustal magma lens continuity and a comparison with first-order and second-order tectonic segmentation. Addressing questions associated with finer scales of segmentation requires a higher sampling density than is currently available. Currently, there also are no seismic investigations of the GEISEIR region to provide a context for the location of possible crustal magma lenses.

The restricted presence of E-MORBs in the SEIR sample suite is relevant to discerning the level of crustal filtering. The occurrence of E-MORBs at a ridge segment center was noted previously along the Mid-Atlantic Ridge [*Gale et al.*, 2011]. In that case, they were associated with transitional type basalts that occur throughout the ridge segment, and this cooccurrence was interpreted to reflect temporal variability with the E-MORBs derived from an earlier pulse of magmatism [*Gale et al.*, 2011]. Temporal changes in erupted magma composition must also occur along the SEIR, but our understanding of these changes is very limited. Given the present

observations it seems likely this temporal variability is subordinate to mantle melting effects in producing much of the $^{3}He/^{4}He$ variation. Nearly the full range in $^{3}He/^{4}He$ is found over a distance of 10 km in the case of the C17 basalts, and a number of the most depleted MORBs along the SEIR also come from the area immediately adjacent to the E-MORB locations. Given our sampling density, it seems likely that spatial variability in $^{3}He/^{4}He$ associated with the different MORB types (Figures 4 and 5) results from quasi-discrete vertical supply of melt from the mantle to crust. Although there is considerable uncertainty in the amount of filtering by crustal magmatic processes, an issue that requires further evaluation through major and trace element modeling, these crustal-scale processes currently appear to be of lesser importance in controlling the helium isotope variability along the SEIR than melting of the underlying heterogeneous mantle. In this context, we do note that the dominant $^{3}He/^{4}He$-K/Ti relationship for SEIR basalts is a large variability of $^{3}He/^{4}He$ at low K/Ti, while most of the higher K/Ti lavas have low $^{3}He/^{4}He$ ratios (Figure 5b). Mixing of depleted and enriched magmas, in which the depleted magma end-member has a wider range of He concentrations relative to the enriched magma, could lead to large variability in $^{3}He/^{4}He$ at low and relatively uniform K/Ti. One possible cause might be protracted storage and degassing of volumetrically more abundant depleted magmas in the crust, and the occasional intrusion and mixing with enriched magmas. This idea can be further evaluated when additional volatile data (CO_2 and Ar concentrations, plus Ar isotopes) become available.

4.3. Isotope Geochemistry of the Indian Ocean Mantle

The full database for He, Pb, and Hf isotopes in SEIR basalts is provided in the supporting information (Table S1) where the along-axis variations in Pb and Hf isotopes are compared to those for $^{3}He/^{4}He$ (Figure S1).

4.3.1. He-Pb-Hf-Nd-Sr Isotope Relations

Figure 6 displays the relations between $^{3}He/^{4}He$ and selected radiogenic isotope ratios of Pb and Hf for the same samples from the Southeast Indian Ridge. The isotope relationships show several features, including:

1. Overall, the full data SEIR set shows no systematic relationships between He isotopes and those of Pb or Hf.

2. The ocean island and ridge localities having high $^{3}He/^{4}He$ ratios show a considerable range in the isotope compositions of Pb and Hf. All SEIR lavas west of the AAD have a DUPAL signature [*Hart*, 1984] based on their elevated $^{208}Pb/^{206}Pb$ ratios [*Mahoney et al*., 2002].

3. The highest $^{3}He/^{4}He$ ratios extend to 18 R_A and occur at the distant Heard Island/Kerguelen Plateau hot spot, >1500 km from the SEIR. Lower ratios (8–10 R_A) are also observed at those localities. $^{3}He/^{4}He$ ratios are bimodal at Heard Island, with high values in the Laurens Peninsula volcanic series and low values in the Big Ben volcanic series [*Hilton et al*., 1995].

4. Elevated $^{3}He/^{4}He$ ratios, >14 R_A, are also associated with the Amsterdam-St. Paul hot spot which influences ridge segments atop and immediately northwest of the ASP Plateau [*Graham et al*., 1999]. Along some of these segments the isotope trends involving He approximate binary mixtures but they can have distinctly different Sr-Nd-Pb-Hf isotope compositions for the hot spot (high-$^{3}He/^{4}He$) end-member [*Nicolaysen et al*., 2007] (cf. segment H versus the ASP segments in Figure 6).

5. Neglecting the E-MORBs along segment C17, basalts from segments L and C17 in the western sector of the GEISEIR area show a slightly increasing trend of $^{3}He/^{4}He$ with radiogenic Pb isotope ratios (Figure 6). These trends along L and C17 could be viewed as extensions of the He-Pb isotope trends produced by mixing with the high-$^{3}He/^{4}He$ ASP hot spot (as exhibited by segments H and those atop the ASP plateau), but extending to even more depleted mantle compositions than are found near the hot spot. However, segments L and C17 are located ~1000 km away and there is little if any overlap in Sr-Nd-Pb-Hf isotope space between these different groupings, which makes a contiguous trend linking them questionable. In this context, based on Pb-Nd-Sr isotope variations in the vicinity of segments L and C17, *Mahoney et al*. [2002] suggested there was little if any mantle flow from the ASP or Kerguelen-Heard hot spots toward the eastern SEIR. The eastward changes in some isotopic parameters are in fact the opposite of those expected from hot spot material flowing into and mixing with depleted MORB mantle beneath the ridge axis.

6. The E-MORBs along segment C17 having high K/Ti (e.g., GSR1 DR B3 highlighted in green in Figure 6) lie away from any possible He-Pb-Hf isotope trends shown by other basalts from the same ridge segment. The E-MORBs are similar in He and Hf isotope compositions to some lavas from Heard Island and Kerguelen (Figure 6), and to the anomalous basalt MD34 D5 from the Southwest Indian Ridge (Table 1). This indicates that

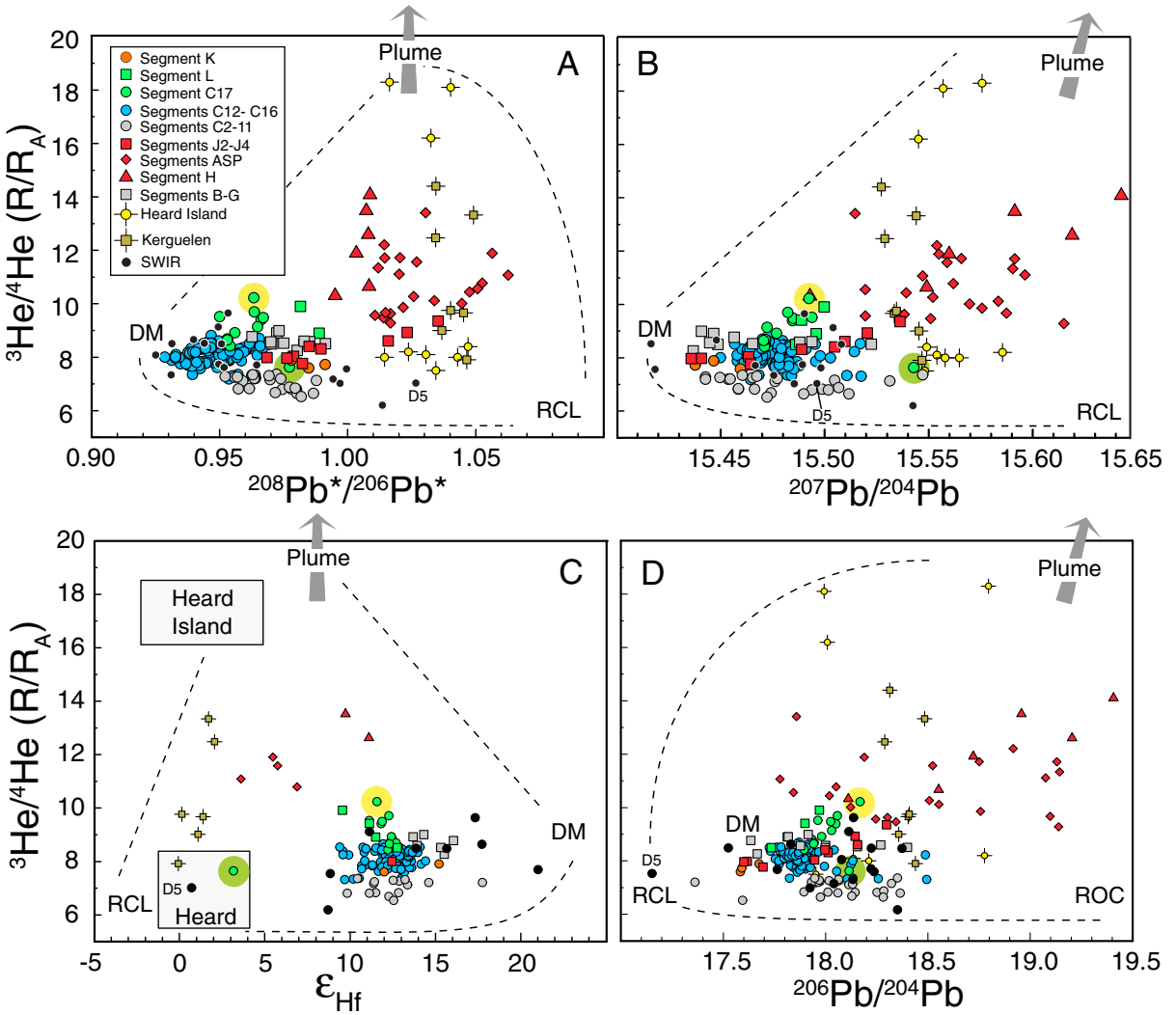

Figure 6. $^{3}He/^{4}He$ versus (a) $^{208}Pb^*/^{206}Pb^*$, (b) $^{207}Pb/^{204}Pb$, (c) ε_{Hf}, and (d) $^{206}Pb/^{204}Pb$. The two highlighted samples are the enriched basalt GSR I DR-B3-1 (green) and the depleted basalt WW10 66-9 (yellow) from segment C17 that are separated by <10 km. Data are from this study, plus *Graham et al.* [1999, 2001, 2006], *Hamelin and Allègre* [1985], *Mahoney et al.* [1989, 1992, 2002], *Johnson et al.* [2000], *Janney et al.* [2005], *Nicolaysen et al.* [2007], and *Hanan et al.* [2013]. The full SEIR isotopic data set is reported in the supporting information (Table S1). Heard Island data are from *Barling and Goldstein* [1990], *Hilton et al.* [1995], and *Barling et al.* [1994]. Because Hf isotope compositions have not been reported for the same samples from Heard Island analyzed for $^{3}He/^{4}He$, the range of expected compositions for the Big Ben (high $^{3}He/^{4}He$) and Laurens Peninsula (low $^{3}He/^{4}He$) volcanic series were estimated from Nd isotopes and the global Hf-Nd isotope correlation, and are shown as boxes. Kerguelen picrite and high-MgO basalt data are from *Doucet et al.* [2005, 2006]. Where their olivine separated from individual samples was analyzed multiple times the $^{3}He/^{4}He$ results have been averaged. Approximate mantle end-members are shown as Plume (having elevated $^{3}He/^{4}He$ but not necessarily the most extreme Pb and Hf isotope compositions, due to multicomponent mixing with recycled materials), DM (depleted mantle), RCL (recycled subcontinental lithosphere), and ROC (recycled ocean crust/subduction mantle wedge).

basalt K/Ti enrichment along the SEIR results from melting of mantle containing ancient heterogeneities that vary significantly in their abundance over length scales of 10 km or less.

7. Samples from the SWIR are few in number (Table 1) but they show both elevated (>9 R_A) and low (<7 R_A) $^{3}He/^{4}He$ ratios. These SWIR samples resemble some of the SEIR basalts, most notably the depleted and enriched MORBs from segments L and C17. In particular, sample MD34 D5 resembles the E-MORBs from C17 (DR B3) in both its low $^{3}He/^{4}He$ (~7 R_A) and low ε_{Hf}. The SWIR D5 sample carries the well-known extremely low-$^{206}Pb/^{204}Pb$ composition measured in some Indian MORBs (Figure 6), as well as characteristically low ε_{Nd} and ε_{Hf} [*Hamelin and Allègre*, 1985; *Mahoney et al.*, 1992; *Chauvel and Blichert-Toft*, 2001; *Janney et al.*, 2005]. Previous work by *Mahoney et al.* [1992] showed that the SWIR segment from which MD34 D5 was recovered, between 39°S and 41°S, represents a tectonic corridor containing stranded fragments of continental lithosphere derived by thermal erosion beneath Madagascar during the mid-Cretaceous.

4.3.2. Melting of Isotopically Heterogeneous Mantle and $^3He/^4He$ in SEIR Basalts

Collectively, the relations involving $^3He/^4He$ shown in Figure 6 show that the low-$^3He/^4He$ signature in the E-MORBs cannot be explained by derivation from an older blob of plume-derived (initially high-$^3He/^4He$) mantle that was passively entrained into the upper mantle flow. While old blobs would be expected to show a negligible aging effect in $^{207}Pb/^{204}Pb$, the E-MORB D3B-1 having low $^3He/^4He$ also has very low ε_{Hf}, and significantly higher $^{208}Pb^*/^{206}Pb^*$ than other basalts from the same ridge segment. This suggests that the low $^3He/^4He$ is a signature of ancient (U+Th)/He fractionation. However, whether $^3He/^4He$ of 7.5 R_A reflects the end-member composition of the heterogeneity giving rise to the E-MORB signature is uncertain. The in situ $^3He/^4He$ ratio could be significantly lower than this value, because the extent to which the $^3He/^4He$ in a basalt reflects a discrete mantle heterogeneity depends on the size of the heterogeneity relative to the volume of mantle sampled during the melting process. This volume may be significantly larger for He than for lithophile tracers such as Hf and Pb, which have diffusivities in mantle phases that are 10^3-10^5 times smaller than He at typical temperatures for the upper mantle (1300–1400°C; see *Hart et al*. [2008] for discussion). This means that as melt transport evolves from a tree-like structure at the base of the melting regime [*Hart*, 1993] upward to the hydrofracture/diking regime, the volume of solid mantle sampled for He can be larger by two orders of magnitude or more (i.e., approximately the reciprocal of the square root of the diffusivity ratio, $\sim(10^4)^{1/2}$). The process is complex because other factors are also important, including the size of the heterogeneity, the relative concentrations of He versus Pb and Hf in the surrounding depleted mantle and in the enriched heterogeneity, stretching and folding of the heterogeneity during solid state deformation, the geometry of melting, the melting rate of the heterogeneity versus surrounding peridotite, and magma ascent rate. *Hart et al*. [2008] showed that the diffusivity of helium prevents long-term survival ($>10^9$ years) of a closed system He isotope signature within radiogenically modified material when it is smaller than a few kilometers. However, the effect of a small heterogeneity on the ambient mantle can persist for long time periods. The extreme He-Pb-Hf isotope signatures for the E-MORBs along segment C17 occur over a distance of <10 km, and are consistent with the presence of a small, ancient (10^8-10^9 years) heterogeneity in the underlying mantle. This heterogeneity is embedded in depleted mantle peridotite but it is enriched in K, U, and Th. For a slab geometry with a thickness of ≤ 1 km, the distance over which diffusion produces a lower $^3He/^4He$ in the ambient mantle is <5 km when $D_{He} = 10^{-10}$ m^2/s and times are in excess of 200 Myr [*Hart et al*., 2008]. This leads to $^3He/^4He$ of $\sim$7.5 R_A for melts sampled over a distance of 10 km or less, similar to the E-MORBs erupted along segment C17.

Differences in the volume of mantle equilibration for He versus lithophile elements during the melt generation process also extend to the presence of refractory mantle domains. Such refractory domains might be produced by ancient melting events and have been hypothesized to be distributed within the upper mantle based on ancient Os isotope model ages in abyssal peridotites [*Harvey et al*., 2006; *Liu et al*., 2008]. These refractory domains would be carried passively in the upper mantle flow field and interwoven with both enriched (recycled) heterogeneities and fertile (lherzolitic) upper mantle but they might not typically contribute to melt generation. In addition, *Salters et al*. [2011] observed different stacked subparallel Hf-Nd isotope arrays for individual sections of the global ridge system which they suggested originate through incongruent melting of mantle with a variable lithological makeup. When a heterogeneous mixture comprised of lherzolite, recyled mafic crust and refractory depleted mantle/recycled lithosphere undergoes melting (with each having a different solidus temperature), the refractory component contributes lithophile elements through melt-rock reaction rather than via directly producing melt. Given that the volume sampled for helium is $\geq$100 times that for lithophile elements during melting, if such refractory domains are present then they will be most effectively sampled for $^3He/^4He$ compared to any other isotopic tracer. The possible bimodal $^3He/^4He$ distribution in Figure 3 takes on added significance in this regard. The two $^3He/^4He$ subpopulations may represent magmas generated from peridotite + pyroxenite melting (<9 R_A) versus pyroxenite-free melting (>9 R_A).

4.3.3. Origin and Distribution of Isotopic Heterogeneity Beneath the SEIR

We attribute the lower $^3He/^4He$ signatures observed in our study area, and much of the variability downward from $^3He/^4He \sim 9$ R_A, to the influence of melting of streaks of enriched mantle embedded within upper mantle peridotite. This enriched material may have a recycled origin, such as ancient subducted ocean crust. It may have also been generated during rift initiation and continental breakup as delaminated lithospheric mantle/lower crust [*Mahoney et al*., 1992; *Janney et al*., 2005; *Hanan et al*., 2004, 2013], or as

small-degree melts trapped in the upper mantle [*Mahoney et al*., 2002; *Russo et al*., 2009]. The low ε_{Hf} of samples such as GSR I D3B-1 and the He-Hf-Pb isotope relations (Figure 6) point to the involvement of recycled continental lithosphere. Much of this material was incorporated during the rifting of Gondwana at 180 Ma and in association with mantle plume-continental lithosphere interaction during the eruption of the Karoo flood basalt province [*Janney et al*., 2005; *Hanan et al*., 2013]. This continental component can also be marked by relatively low $^{206}Pb/^{204}Pb$, exemplified best by the MD34 D5 sample (Figure 6), although in the case of GSR I D3B-1 its $^{206}Pb/^{204}Pb$ is not distinct from the surrounding MORBs on segment C17 despite its very low ε_{Hf} [*Hanan et al*., 2013]. The most radiogenic Pb isotope signatures, notably the elevated $^{206}Pb/^{204}Pb$ (up to 19.6) and $^{207}Pb/^{204}Pb$ (up to 15.67) in the vicinity of the ASP plateau [*Doucet et al*., 2004; *Nicolaysen et al*., 2007; *Janin et al*., 2012], are commonly associated with recycled ocean crust [*Hanan and Graham*, 1996], or with mantle wedge that was contaminated with melts during subduction [*Donnelly et al*., 2004]. In those cases where the SEIR lavas show this radiogenic Pb isotope signature most strongly, they have elevated $^{3}He/^{4}He$ rather than the low ratios expected from the presence of ancient recycled material. This may be accounted for by hybridization of streaks of the recycled material with deep, less degassed mantle. For basalts from the Austral Islands, *Parai et al*. [2009] showed that nucleogenic $^{21}Ne/^{22}Ne$ correlates with radiogenic Pb (designated HIMU by *Zindler and Hart* [1986]), but the source $^{21}Ne/^{22}Ne$ is lower than for the depleted upper mantle and resembles values for less degassed mantle. *Parai et al*. [2009] therefore suggested that the recycled material responsible for the radiogenic Pb isotope signature behaves as an open system, acquiring a large part of its noble gas signature from equilibration with the surrounding deep mantle ($^{3}He/^{4}He$ at HIMU localities is typically lower than in MORBs, between 5–7 R_A) [*Graham et al*., 1992; *Hanyu and Kaneoka*, 1998; *Hanyu et al*., 1999; *Parai et al*., 2009]. The ***C*** isotope signature of the ASP hot spot is not as radiogenic in its Pb isotope character as the HIMU signature of the Australs due to its younger recycling age (Proterozoic or younger for ***C*** versus Archean for HIMU: *Hanan and Graham* [1996]; *Cabral et al*. [2013]). We suggest that the *Hanyu and Kaneoka* [1998] and *Parai et al*. [2009] model can be extended to account for the cooccurrence of elevated $^{3}He/^{4}He$ in the ASP-influenced lavas having radiogenic Pb isotope compositions.

The present He isotope results considered in light of the isotope variations in Pb-Hf-Nd-Sr therefore indicate the involvement of four discernible geochemical end-members. These components are depleted (ambient) upper mantle, recycled ocean crust/mantle wedge (***C*** component), a deep plume component (having elevated $^{3}He/^{4}He$), and recycled continental lithosphere (distinguished most readily by low ε_{Hf}).

A cartoon of the mantle flow field responsible for the isotope signatures along the SEIR is shown in Figure 7. One possibility is that small domains (blobs) of plume material escape the deep upwelling beneath the ASP Plateau and eventually become incorporated into the melting region ~1000 km away beneath segments L and C17. While we cannot exclude this model due to possible temporal variability in blob compositions associated with hot spot volcanism, we do not favor it because it does not accurately account for the collective Sr-Nd-Pb isotope characteristics of the lavas in the 88°E region of the SEIR [*Mahoney et al*., 2002]. A more plausible model is the rare injection of blobs from the mantle transition zone or deeper mantle, which become passively entrained into the upper mantle flow. In this regard, it is noteworthy that the dominant wavelength of the He isotopic features along the SEIR is ~1000 km (see below). This length scale resembles that for undulating, low-viscosity plume-like features deduced from seismic tomography that are present near 400 km depth and rooted in the deep mantle [*French et al*., 2013].

4.4. Spectral Analysis of the Length Scales of Helium Isotope Variability

Upper mantle heterogeneities originate through continuous mantle differentiation over Earth history and are acted upon by mantle stirring. Below we adopt a comparative strategy to deduce quantitatively the scales of these heterogeneities in the upper mantle. Because the local isotopic composition of the mantle depends mainly on the advection of heterogeneities by the mantle flow field [*Richter and Ribe*, 1979], our analysis has implications for mantle convective processes. This convection is vigorous on geological timescales (occurring at high Rayleigh number), three dimensional and time dependent. It is forced at plate scales but nonlinear interactions can spread the energy out over a range of intermediate and smaller scales. To evaluate the length scales of helium isotope variability in a quantitative way, we adopted four different approaches; (1) the periodogram [*Lomb*, 1976; *Scargle*, 1982], (2) red-noise spectral estimation (REDFIT of *Schulz and Mudelsee* [2002]), (3) the multitaper method (MTM) of spectrum estimation [*Thomson*, 1982; *Lees and Park*, 1995], and (4) continuous wavelet transform [*Grinsted et al*., 2004]. Details are described in the supporting information.

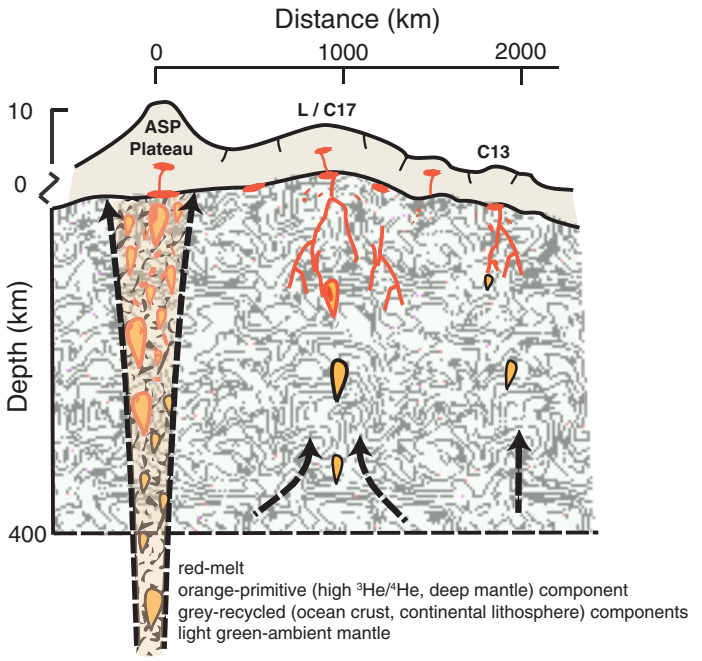

Figure 7. A cartoon of one possible model for mantle heterogeneity, mantle flow, and melting beneath the SEIR. Length scales are approximate. Note the break in scale between the crust and mantle. The light background depicts ambient mantle (peridotite) and orange depicts domains of mantle having elevated $^{3}He/^{4}He$ (>15 R_A, as measured at the ASP Plateau) that are ultimately derived from the deep mantle. Gray folded strands depict ancient components, either recycled (continental and oceanic) lithosphere or frozen melt (trapped during initial ocean basin rifting), attested to by the isotope relationships for Hf-Pb-Sr-Nd described in *Mahoney et al.* [2002], *Nicolaysen et al.* [2007], *Graham et al.* [2006], and *Hanan et al.* [2013]. Red depicts melt and is highly schematic.

4.4.1. Periodogram

Periodogram analysis of the isotope variations along mid-ocean ridges from the Atlantic Ocean was previously shown to contain two spectral types [*Agranier et al.*, 2005]. The first is a hot spot type, containing distinct lobes at low wave number k (large distance), plus a sharp cutoff near k∼0.2 $(°)^{-1}$ (∼550 km). Beyond this wave number (at higher frequency), the signal appeared to be dominated by white noise. This spectral type is exhibited by $^{3}He/^{4}He$, $^{87}Sr/^{86}Sr$, and $^{206}Pb/^{204}Pb$ [*Agranier et al.*, 2005] along mid-ocean ridges from the Atlantic. The second spectral type was referred to as the Batchelor regime. It exhibits a long-wavelength structure similar to type 1, but it has a continuous decrease with increasing wave number (which can be approximated by a power law exponent of −1). This spectral type is exhibited by Nd and Hf isotopes, and the second component of a Pb isotope principal component analysis [*Agranier et al.*, 2005]. The type 2 spectrum was hypothesized to be produced by continual reduction in the size of mantle heterogeneities caused by the stretching and refolding that occurs during mantle convection.

The Lomb-Scargle periodogram for $^{3}He/^{4}He$ variations along the SEIR is shown in Figure 8. We performed the analysis using the full SEIR data set (248 sample locations), data from the GEISEIR I and II study area (81°E–101°E, 179 locations), and the most densely sampled area (89.7°E–101°E, 111 locations). Similar to what was observed previously along the Mid-Atlantic Ridge [*Agranier et al.*, 2005], lobes are present for $^{3}He/^{4}He$ at wave numbers of 0.001 and 0.002 km^{-1} (∼1000 and 500 km, respectively) in both the full data set and the GEISEIR study region. In the most densely sampled region (Figure 8c), the periodogram also begins to reveal possible structures at larger wave number (0.003 and 0.004, i.e., ∼330 and 250 km, respectively). It is difficult to interpret the meaning of the higher wave number peaks in Figure 8c as they do not appear to be statistically significant in the full data analysis. They may be artificial overtones of the lower wave number peaks near 1000 and 500 km.

4.4.2. Red-Noise Spectral Estimation (REDFIT)

Figure 9 shows a REDFIT analysis of $^{3}He/^{4}He$ along the SEIR. The data have been analyzed in two ways. The first treatment focuses on the GEISEIR I and II study region (n = 172), while the second is for the full data set (248 sample locations). The results in Figure 9 were obtained using an overlapping segment approach, but other choices for number of segments and window shape (rectangular, triangular) did not produce outcomes that were significantly different. The results of this analysis reveal a significant peak at large length scale. For the full data set, this power is mostly concentrated in a ∼1000 km peak (significant at >99% confidence level), much like the Lomb-Scargle periodogram. An ∼500 km peak is also present in this case but it is not as statistically significant (Figure 9b). Significant (>95% confidence level) peaks are also observed in the full data set at length scales of ∼50–70 km. For the more restricted, densely sampled data (1825 km of ridge, see Figure 9a) the 500 km peak is significant at the 99% confidence level. Peaks are significant at

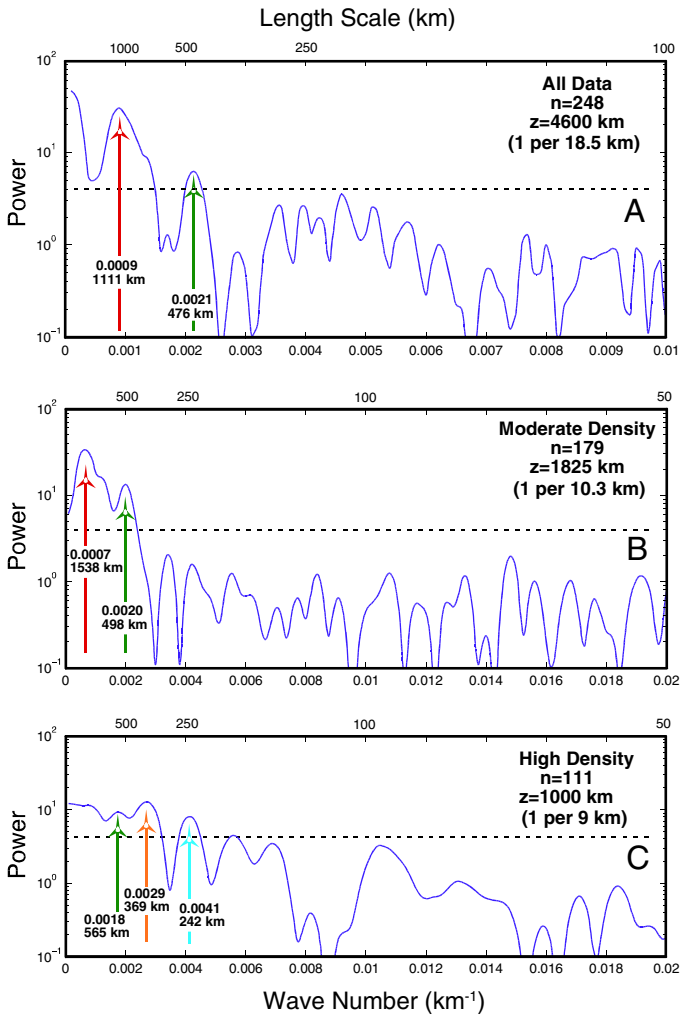

Figure 8. Periodograms of the SEIR $^3He/^4He$ variations. (a) All Data (248 locations). (b) Samples from 80.98°E–101°E (179 locations). (c) Samples from 89.69°E–101°E (111 locations). The dashed lines represent the 95% confidence level above which the peaks in the spectrum are deemed significant.

~500 and ~30 km for the densely sampled region. Overall, the REDFIT results resemble those obtained from the periodogram analysis. Notably, when only the GEISEIR study area is considered we observe a statistically significant peak near 30 km, identical to the characteristic length scale deduced from the bimodal distribution of Hf and Pb isotopes in the GEISEIR I region [*Hanan et al*., 2013].

4.4.3. Multitaper Method (MTM) of Spectral Estimation

Application of MTM requires equally spaced data. To achieve this, we preprocessed the helium isotope data series utilizing a Gaussian interpolation applied over three different subsets of the data in order to reduce effects of aliasing plus any data gaps on spectral estimation. The preprocessing is illustrated graphically in Figure 10a. In treatment (a), the He isotope data were interpolated along-axis between −300 and +3140 km at an interval i of 40 km using a Gaussian half-width w of 60 km. The total number of interpolated locations n is 87. In (b), the along-axis distance ranged from 380 to 2140 km, w = 40 km, i = 20 km, and n = 89. In (c), the along-axis distance ranged from 700 to 2010 km, w = 20 km, i = 10 km, and n = 132. The application of the Gaussian filter leads to a relatively sharp cutoff in spectral estimation at a wave number between the full-width and half-width. Examples for the estimated power spectrum and F-test values for each of the three cases (case (a) using five tapers, cases (b) and (c) using three tapers) are illustrated in Figures 10b–10d.

For the longest part of the data series (subset a), the spectrum estimation reveals periodicities in relative power at ~1000 and ~500 km (Figure 10b). The 500 km peak is not well resolved in this estimation of the spectrum but the F-value suggests it is significant at >95% confidence. Although a broad spectral peak also occurs near 200 km, it is not statistically significant. Elevated F-values also occur at higher wave number (wave number ~0.4, length scale ~100 km) but this is close to the Gaussian filter cutoff length scale (60–120 km) and the associated spectral peaks are also quite subdued. The occurrence of relatively high F-values at higher wave number where peaks are absent in the spectrum can be caused by random noise related to peculiarities in sampling [*Lees and Park*, 1995]. From case (a), we conclude that significant power is found in the overall data series at ~1000 km, while a weaker peak may also be present near 500 km.

Spectrum estimation for the shorter treatments of the data series (subsets b and c) reveal significant relative power at a length scale between ~425 and ~650 km in each case (Figures 10c and 10d). Evidence for an

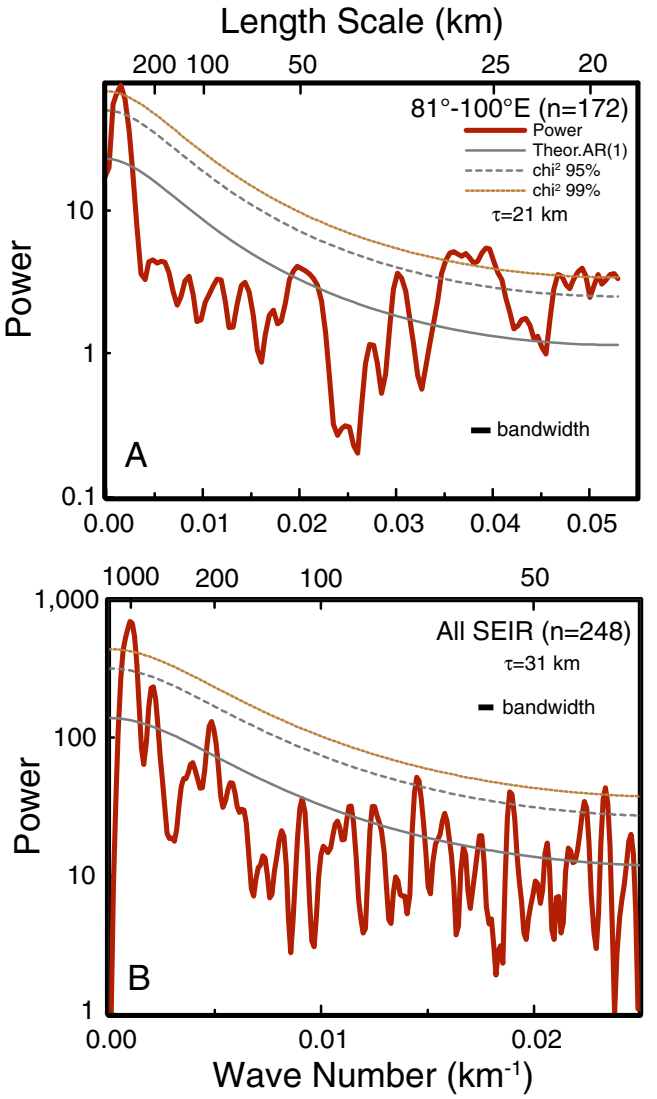

Figure 9. Red-noise spectral estimation for $^3He/^4He$ (after *Schulz and Mudelsee* [2002]). (a) Upper plot shows results for the densely sampled portion of the SEIR (z = 1825 km, from 80.98°E–100°E; n = 172 locations). (b) Lower plot shows results for all SEIR data (z = 4600 km, n = 248 locations). Power is expressed in units proportional to the square of the amplitudes of the sinusoids present in the data. The illustrated example uses a Welch overlapping segment average (WOSA) with 50% overlap for each of three segments (see supporting information for details). Other choices for window shape (rectangular, triangular) and number of segments do not produce results very different from those depicted here. For the cases here, in the dense area $\tau = 21$ km with bandwidth = 0.00197 km^{-1}. For all ridge data $\tau = 31$ km and bandwidth = 0.00070 km^{-1}. The solid gray curve depicts the theoretical autoregressive (AR(1)) red-noise model (the null hypothesis against which peak significance is tested). The dashed lines depict 95% and 99% significance levels.

~500 km peak is, therefore, found for all the cases we investigated but it is not well resolved in the treatment using subset (a). The peak near 500 km in the more densely sampled data series suggests it may be a fundamental length scale of He isotope variability in the mantle, rather than a harmonic overtone of the ~1000 km scale that was produced from the choice of data windows or interpolation schemes.

In case (b), the strongest peaks are observed at ~150 and ~100 km, with greater than 99% confidence level for each (Figure 10c). For the most densely sampled case (c) explored here we also observe peaks at ~100 and ~40 km. The latter length scale exhibits the most significance in this case (c) in terms of its high F-value, and it resembles the ~30 km signal previously observed in the REDFIT spectrum estimation using unequally spaced data. This ~40 km peak is also close to the Gaussian filter cutoff length (20–40 km). In addition, in cases (b) and (c), the exact position and significance of the peaks at ~150, ~100, and ~40 km can shift somewhat with the choice of the number of tapers, indicating that the data series show some tendencies to nonstationarity, i.e., they have changing $^3He/^4He$ means and variances along the length of the SEIR. This is an inherent limitation in our ability to make more extensive quantitative arguments from these simple spectral analysis approaches.

We conclude from the MTM analysis that fundamental peaks in the He isotope variability occur along the SEIR at approximately 1000, 500, 150–100, and 40 km length scales.

4.4.4. Continuous Wavelet Transform

We employed the algorithm developed by *Grinsted et al.* [2004] to estimate the CWT for $^3He/^4He$ variations along the SEIR. Data were interpolated at 10 km intervals along the SEIR using a piecewise cubic hermite spline. The CWT for $^3He/^4He$ along the SEIR is shown in Figure 11. Pervasive power is observed at ~1000 and ~500 km length scales along much of the SEIR. These length scales are similar to those discerned from

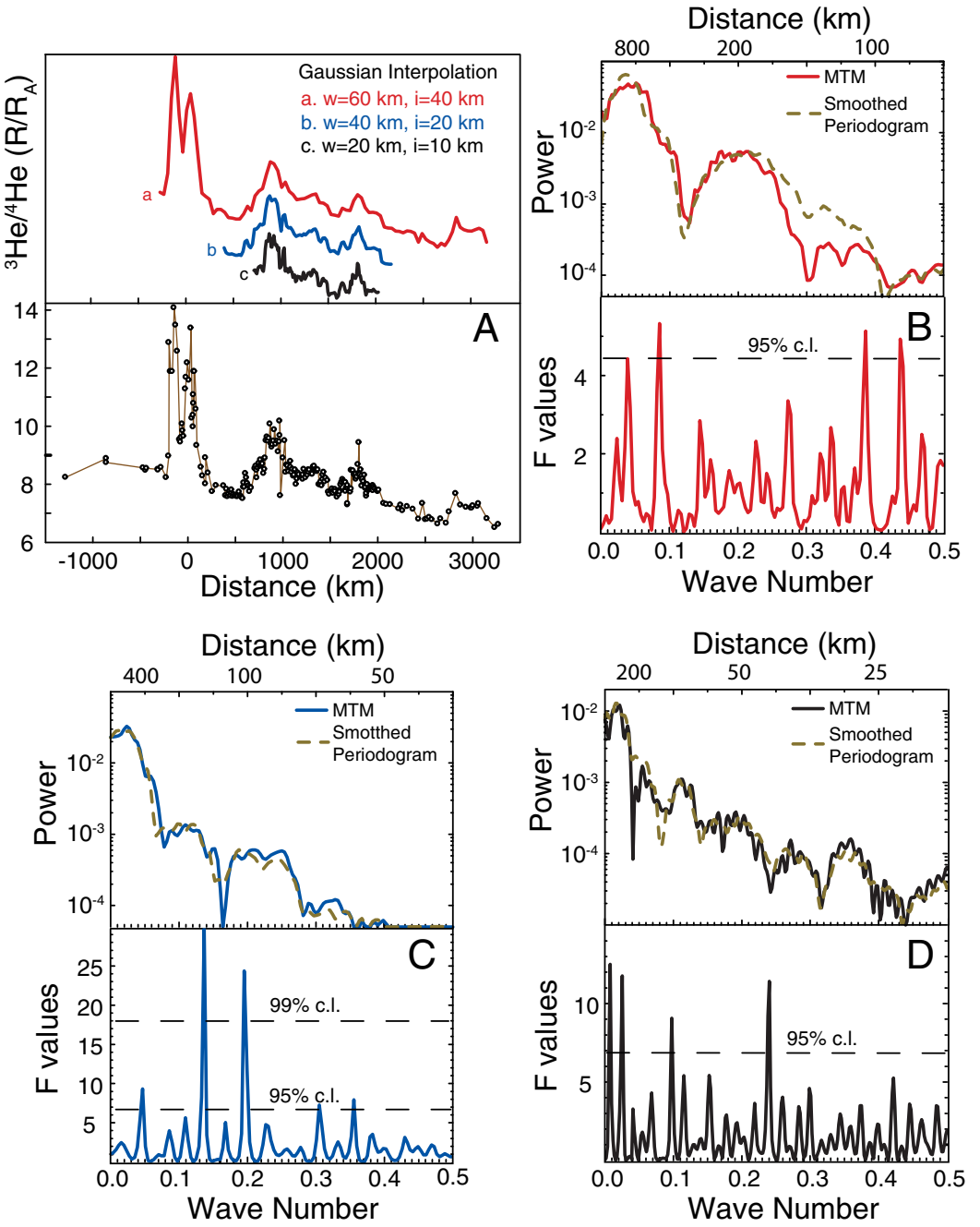

Figure 10. MTM analysis of the SEIR He isotope variations. (a) Gaussian interpolation of the variations. The data series was treated in three different ways. In treatment (a), the He isotope data were interpolated along-axis between −300 and +3140 km, at an interval (i) of 40 km using a Gaussian filter having a half-width (w) of 60 km. The total number of interpolated locations (n) is 87. The MTM applied to treatment (a) shown here utilized five tapers. In treatment (b), the along-axis distance ranged from 380 to 2140 km, w = 40 km, I = 20 km, and n = 89. The MTM applied to treatment (b) shown here utilized three tapers. In treatment (c), the along-axis distance ranged from 700 to 2010, w = 20 km, i = 10 km, and n = 132. The MTM applied to treatment (c) shown here utilized three tapers. (b–d) show the spectrum estimates from the MTM, and the corresponding confidence levels from the computed F-test values. The smoothed periodograms for the same data treatments are shown for comparison. Wave number range is from zero to the Nyquist limit (= sampling interval divided by 0.5), corresponding to 80, 40, and 20 km for series a, b, and c, respectively.

the various periodogram and REDFIT treatments discussed earlier. One advantage of the wavelet analysis is that it provides a depiction of how power at different periods (length scales) is localized across the spatial domain. In addition to the power at ~500 and ~1000 km length scales, the CWT for $^3He/^4He$ displays localized power at length scales of ~75–250 km in the vicinity of the ASP hot spot, and at ~50–100 km for

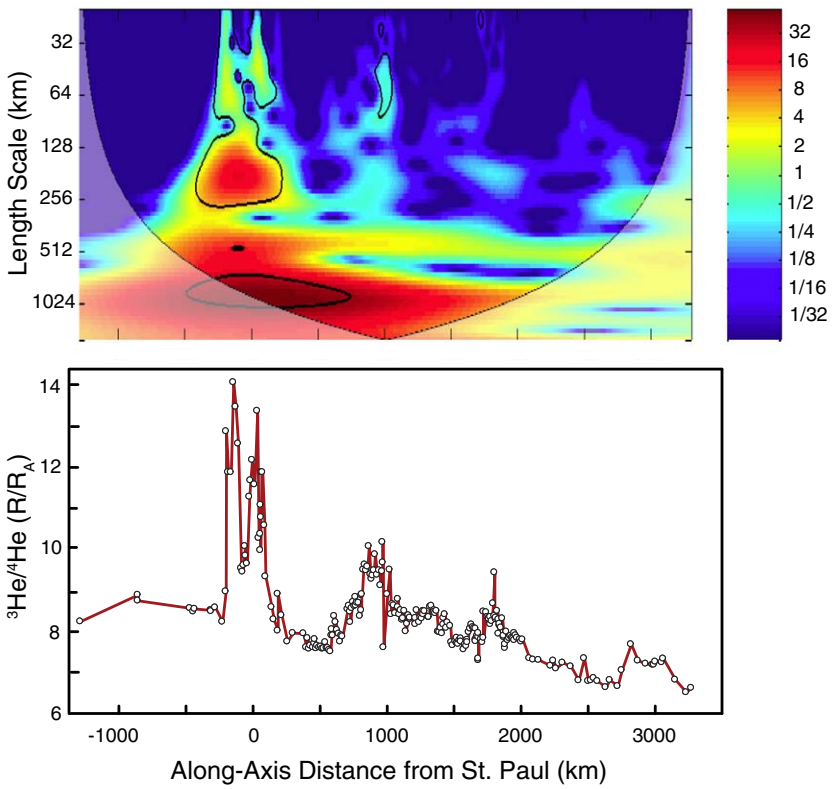

Figure 11. Continuous wavelet transform (CWT) and the ^{3}He/^{4}He variations along the SEIR. The vertical axis on the upper plot is a natural logarithm scale of the length scale (km) with each unit corresponding to a doubling in size. Signal power is displayed in color according to the scale shown at the right. The cone of influence of boundary effects is outlined in gray. Thick contours outline 5% significance levels.

basalts erupted at along-axis distances of ~800–1100 km. This latter area corresponds to the local ^{3}He/^{4}He peak that is clearly visible in the along-axis data itself (Figures 2 and 4).

In our treatment, we also determined the Cross-Wavelet Transform (XWT) and Wavelet Transform Coherence (WTC) between ^{3}He/^{4}He and Pb and Hf isotopes (see supporting information Figures S2–S4) and between ^{3}He/^{4}He and axial depth. These additional visualizations can be used to investigate power and phase relationships between isotopes and bathymetry along the SEIR. The XWT is constructed from two CWT's [*Grinsted et al.*, 2004]. In a case where the XWT phase relationship is locked within a narrow range, it seems likely that variations at that length scale should have a similar mechanistic origin.

Figure 12a shows the XWT between ^{3}He/^{4}He and axial depth. A significant common power is observed at ~500 km and between ~75 and 250 km in the region of the ASP plateau (Figure 12a). At these shorter periods, it is notable that the relationship between He isotopes and axial depth is not simply in-phase or out-of-phase. This contrasts with the ~1000 km length scale along nearly the entire SEIR in which there is a remarkable in-phase relationship (Figure 12a). The WTC is plotted in Figure 12b and helps resolve more clearly the ~1000 and ~500 km scale relationships between He isotopes and axial depth hinted at by the XWT. The ~1000 km length scale coherence pervades the SEIR, although it is rendered less certain close to the boundaries of the sampling domain by the edge effect delineated by the cone of influence (COI). The ~500 km scale encompasses the western one third to one half of the study region. The coherence at 1000 km length scale between ^{3}He/^{4}He and axial depth is well defined in the WTC, while at ~500 km length scale the phase relationship is shifted by about 45°. Local islands of coherence at hundred km length scales may also be present in the distal eastern sections of the SEIR at along-axis distance of ~2500 km (Figure 12b). These long-wavelength scales are similar to the very largest scales of ridge segmentation, which is defined by the persistence of fracture zone anomalies in satellite gravity data [*Small et al.*, 1999]. Those features appear to delineate tectonic corridors that have been stable since ~38 Ma when the SEIR migrated over the Kerguelen hot spot.

The CWT results support our earlier inference based on the periodogram, REDFIT and MTM results that key ^{3}He/^{4}He variability is found at ~1000 and ~500 km length scales. Significant localized variability also occurs

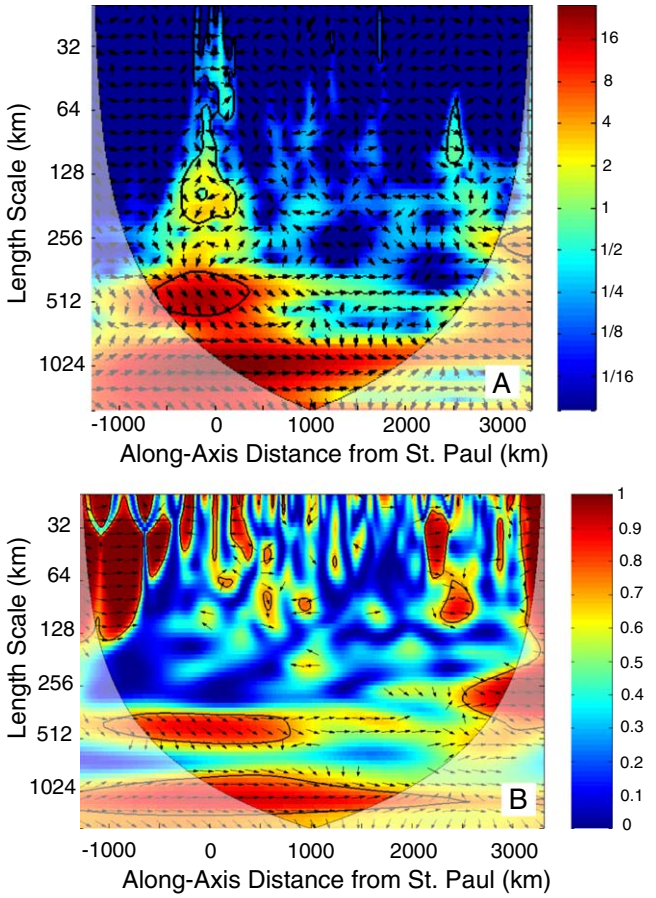

Figure 12. (a) Cross-wavelet transform (XWT) and (b) Wavelet transform coherence (WTC) of ^{3}He/^{4}He and axial depth. The vertical axis is a natural logarithm scale of the length scale (km) with each unit corresponding to a doubling in size. Signal power (a) and coherence (b) are contoured in color according to the scale shown at the right. Arrows depict the phase relationship between ^{3}He/^{4}He and axial depth as a function of length scale (vertical axis) and location along the SEIR (horizontal axis). Right-pointing arrows indicate an in-phase relationship and left-pointing an antiphase relationship. Downward pointing arrows correspond to where axial depth leads ^{3}He/^{4}He, while upward pointing corresponds to where depth lags. Thick contours outline 5% significance levels.

at 75–250 km length scales, primarily in the vicinity of the ASP hot spot and at ~900 km east of St. Paul island.

4.5. Implications for Mantle Convection

4.5.1. ^{3}He/^{4}He Textures in the Upper Mantle

It has been recognized for 30 years that the Indian Ocean upper mantle has a distinct long-term evolutionary history [*Dupré and Allègre*, 1983; *Hart*, 1984; *Hamelin and Allègre*, 1985; *Hamelin et al*., 1986]. The Pb-Nd-Sr isotopic variability for Indian Ridges at a sampling interval of ~50 km was evaluated using the periodogram approach and interpreted by *Meyzen et al*. [2007] to result from a refolded structure produced largely by refilling of the upper mantle through localized upwellings of deep mantle. The involvement of a deep mantle source, inferred in *Meyzen et al*. [2007] and supported by the helium isotope results presented here, is consistent with the common DUPAL nature of both ocean island basalts (OIBs) and MORBs in the Indian Ocean [*Castillo*, 1988]. It is notable, however, that this isotopic flavor is also demonstrably associated with *shallow* recycling of continental lithosphere and/or lower crust elsewhere in the mantle, such as beneath the SWIR, the southern MAR, and the Arctic [*Mahoney et al*., 1992; *Janney et al*., 2005; *Kamenetsky et al*., 2001; *Class and le Roex*, 2006; *Goldstein et al*., 2008].

A basic question up to now has been whether the spectra of mantle heterogeneities beneath the Atlantic [*Agranier et al*., 2005] are different from those beneath the Pacific and Indian oceans. One simple expectation might be that differences would be found that relate to tectonic history of the continents bordering the basins or to the speed of mantle convection and the influence of mantle plumes. The ^{3}He/^{4}He character for the Indian Ocean deduced from the spectral analysis of the SEIR (Figures 8–11) shows peaks near 1000 and 500 km. Because this large length scale resembles that in Atlantic periodograms it supports the notion that these two distinct regions of the upper mantle have similar helium isotopic textures. The similar ^{3}He/^{4}He textures further suggest that upwelling combined with stirring have produced broadly similar He isotope dispersions in the upper mantle around the globe.

4.5.2. A Comparison to the Southern East Pacific Rise

We suggest that ^{3}He/^{4}He variability along the mid-ocean ridge system is marked by a similar long-wavelength character and explore this further by an additional simple comparison. We choose the Pacific because we have already shown through spectral analysis that ridge systems in the Indian and Atlantic Oceans [*Agranier et al*., 2005] have similar long-wavelength He isotope textures. We compare the along-

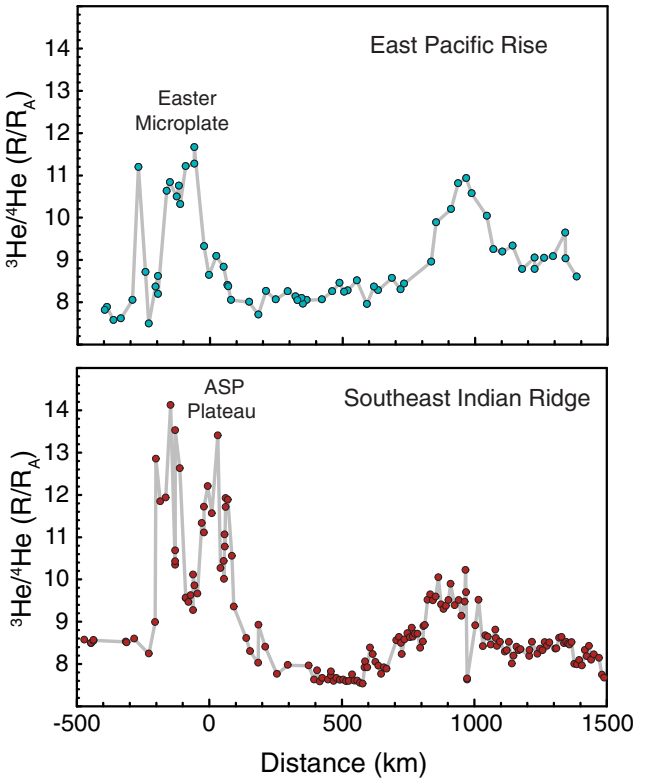

Figure 13. A comparison of MORB He isotope variations from the southern East Pacific Rise and the Southeast Indian Ridge. EPR data are from *Poreda et al.* [1993] and *Kurz et al.* [2005]; SEIR data are from *Graham et al.* [1999, 2001], *Nicolaysen et al.* [2007], and this study.

axis variations for the SEIR with those for a section of the southern East Pacific Rise (Figure 13). Although this ~2000 km long section of the EPR was sampled at approximately 40% of the sampling density of the SEIR, the key long-wavelength features are evident. The selected EPR region encompasses the Easter Microplate where MORB signatures in He-Pb-Sr-Nd-Hf isotopes are influenced by input from the nearby Easter mantle plume [*Hanan and Schilling*, 1989; *Fontignie and Schilling*, 1991; *Poreda et al.*, 1993; *Kingsley et al.*, 2007], analogous to the ASP hot spot along the SEIR. The selected EPR section also includes the superfast-spreading region from 13°S to 23°S with prominent He-Pb-Nd-Sr isotope anomalies [*Mahoney et al.*, 1994; *Kurz et al.*, 2005]. Figure 13 shows a remarkable similarity in both the amplitude and period of the $^3He/^4He$ variations for these regions despite the large difference in their ridge spreading rates.

It could be a simple coincidence that these two sections of the mid-ocean ridge system seem so similar but we consider that unlikely. Each area is marked by the upwelling of a mantle plume (ASP versus Easter) that is sufficiently intense to produce ocean island volcanism. Each ridge section influenced by the nearby mantle plume shows elevated $^3He/^4He$ extending along the ridge for ~300–400 km. Each ridge system also contains a broad auxiliary peak located ~900–1000 km away from the primary hot spot region (the 88°E region of the SEIR versus the superfast EPR). Each auxiliary region has an elevated $^3He/^4He$ anomaly (~10–11 R_A) that is marked by a basal width of ~200–400 km. Increased melt production, expressed as shallower axial depth, plus the presence of several near-axis seamounts in the SEIR case, is also broadly associated with each of these auxiliary regions.

There are also important differences between the two systems when they are compared in detail, and these point to additional complexity. The Easter hot spot is ~500–1000 km away from the ridge axis [*Hanan and Schilling*, 1989], considerably farther than the case for the ASP hot spot (~100 km). The tectonic settings are different, with the Easter Microplate being comprised of two rift branches along its east and west boundaries while the ASP hot spot is located beneath a broad submarine plateau. The $^3He/^4He$ relationships with Pb-Sr-Nd isotopes for each of the auxiliary regions in this comparison is not explained by simple mixing models involving the respective hot spot sources and background MORB mantles [*Mahoney et al.*, 2002; *Kurz et al.*, 2005]. It is further noteworthy that the $^3He/^4He$-K/Ti relationships observed along the SEIR, in which the E-MORB character is associated with lower $^3He/^4He$, differ from those observed for the southern EPR where E-MORBs sometimes carry elevated $^3He/^4He$ [*Kurz et al.*, 2005].

Despite the aforementioned complexities, the SEIR-EPR similarity can be explained by similar auxiliary upwellings from depth. These upwellings may originate from either the lower mantle or deeper parts of the upper mantle, and they appear to be located ~1000 km away from the hot spots interacting with the respective spreading ridge systems. These auxiliary upwellings may be mantle blobs [*Allègre et al.*, 1984;

Gurnis, 1986b; *Manga*, 1996; *Becker et al*., 1999; *Vlastelic et al*., 2002]. If the blob flux to the subridge mantle is relatively low and blob size is of the order of a ridge segment or smaller then significant ^{3}He/^{4}He variability might occur on time scales of 10^6-10^7 years. This resembles the case study for MORBs and near-ridge seamounts in the South Atlantic at 26°S, where ^{3}He/^{4}He along the ridge is low (7.3–7.7 R_A) but older seamount lavas on both sides of the ridge axis extend to 11 R_A [*Graham et al*., 1996]. In this context, the recent waveform seismic tomography study by *French et al*. [2013] also reveals the global presence of undulating, plume-like features that could produce blobs. These features have a wavelength of the order of 10^3 km and are located at ~400 km depth in the upper mantle but apparently are rooted in the deep mantle. They are manifested as low-viscosity fingers and are present beneath the fast moving Pacific Plate where secondary convection rolls are likely to develop, but also beneath the slower moving Atlantic and Indian Plates where the presence of such rolls was thought to be unlikely.

5. Conclusions

The SEIR is a regional-scale analogue of the global mid-ocean ridge system, and was previously known to show significant isotopic variability due to ancient heterogeneities embedded in the upper mantle. A new sample suite, collected at 5–10 km intervals for a distance of >1600 km between 81°E and 100°E, shows a ^{3}He/^{4}He range from 7.5 to 10.2 R_A that encompasses more than half the known range in MORBs erupted away from ocean island hot spots. Abrupt transitions occur in this record over lateral distances of 10 km or less, indicating significant small-scale (<10 km) helium isotope variability in the upper mantle beneath the SEIR. The higher ^{3}He/^{4}He ratios in this densely sampled region are associated with depleted MORB compositions (low K/Ti), while the lower ^{3}He/^{4}He ratios are associated with E-MORB compositions (K/Ti > 0.2).

Relations between ^{3}He/^{4}He and the radiogenic isotopes of Pb and Hf reveal that the E-MORB He isotope signature is related to melting of ancient mantle heterogeneities that originated as recycled continental and oceanic lithosphere, or as incipient melts trapped during continental rifting and the early stages of opening of the Indian Ocean basin. Collectively the isotopes indicate involvement of at least four distinct mantle end-members; depleted upper mantle peridotite, a deeply derived plume component (spatially restricted to the influence of the Amsterdam-St. Paul hot spot), and recycled continental and oceanic lithosphere. Melting of mantle containing a few percent garnet pyroxenite or eclogite leads to lower ^{3}He/^{4}He ratios, while ^{3}He/^{4}He ratios above ~9 R_A may arise from melting of pyroxenite-free or eclogite-free mantle.

Spectral analysis of the He isotope variations reveals strong peaks at ~1000 and ~500 km, and less prominent peaks at ~100–150 km and 30–40 km. Mesoscale flow features in the mantle may account for the ~100–150 km length scales. The ~30–40 km length scale is identical to that deduced from Hf and Pb isotope variations in the same sample suite, and appears best accounted for by melting of eclogite or garnet pyroxenite that is heterogeneously distributed within the subridge mantle. The longest wavelength features of ^{3}He/^{4}He variability in the Indian Ocean upper mantle resemble those beneath the Atlantic Ocean, previously described as a hot spot-type spectrum. ^{3}He/^{4}He variations along the SEIR are also remarkably similar in amplitude and wavelength to those along the southern East Pacific Rise. The ^{3}He/^{4}He and axial-depth variations along the SEIR are highly coherent at 500–1000 km. This indicates a close coupling between melt production and ^{3}He/^{4}He, probably due to regional variations in upper mantle temperature driven by thermal upwelling from depth.

Acknowledgments

This paper is dedicated to the memory of John Mahoney. D.G. and B.H. were supported by the Marine Geology & Geophysics program of the U.S. National Science Foundation. The OSU Noble Gas Lab was established through a Major Research Instrumentation grant from MG&G. The Keck Foundation contributed to establishment of the Isotope Geochemistry clean rooms at SDSU. J.B.T. and F.A. received support from the French Agence Nationale de la Recherche (grant ANR-10-BLAN-0603 M&Ms—Mantle Melting—Measurements, Models, Mechanisms). C.H. acknowledges the French Institut Paul Emile Victor (IPEV) for ship time and staff onboard the ship, and the French Institut National des Sciences de l'Univers for financial support through the program Campagne à la mer. Anne Briais and Marcia Maia provided superb bathymetric mapping plus magnetics and gravity expertise during GEISEIR I and II that led to the highly successful rock sampling of the ridge axis. We are grateful to captains F. Duchêne and C. Garzon of the R/V Marion Dufresne, and their crews during the MD171 (GEISEIR I) and MD175 (GEISEIR II) scientific expeditions. Figure 1 was produced using GeoMapApp (http://www.marine-geo.org/geomapapp), which is supported by the National Science Foundation and internal funding from Lamont-Doherty Earth Observatory. Some data analysis was carried out using computer software written for MATLAB® plus the PAST software package (**PA**leontological **St**atistics, available at http://folk.uio.no/ohammer/past/; *Hammer et al*. [2001]). We thank Frank Spera and John Lupton for valuable discussions, Alan Mix for providing the Gaussian interpolation software and help with many aspects of the spectral analysis, and Sujoy Mukhopadhyay and an anonymous reviewer for constructive reviews.

References

Agranier, A., J. Blichert-Toft, D. W. Graham, V. Debaille, P. Schiano, and F. Albarede (2005), The spectra of isotopic heterogeneities along the Mid-Atlantic Ridge, *Earth Planet. Sci. Lett.*, *238*, 96–109.

Albarède, F. (2005), The survival of mantle geochemical heterogeneities, in *Earth's Deep Mantle: Structure, Composition and Evolution*, edited by R. D. van der Hilst, J. Bass, J. Matas, and J. Trampert, pp. 27–46, AGU, Washington, D. C.

Allègre, C. J., and D. L. Turcotte (1986), Implications of a two-component marble-cake mantle, *Nature*, *323*, 123–127.

Allègre, C. J., O. Brévart, B. Dupré, and J.-F. Minster (1980), Isotopic and chemical effects produced in a continuously differentiating convecting Earth mantle, *Philos. Trans. R. Soc. London A*, *297*, 447–477.

Allègre, C. J., B. Hamelin, and B. Dupré (1984), Statistical analysis of isotopic ratios in MORB: The mantle blob cluster model and the convective regime of the mantle, *Earth Planet. Sci. Lett.*, *71*, 71–84.

Anderson, D. L. (2006), Speculations on the nature and cause of mantle heterogeneity, *Tectonophysics*, *416*, 7–22.

Baran, J. M., J. R. Cochran, S. M. Carbotte, and M. R. Nedimovic (2005), Variations in upper crustal structure due to variable mantle temperature along the Southeast Indian Ridge, *Geochem. Geophys. Geosyst.*, *6*, Q11002, doi:10.1029/2005GC000943.

Barling, J., and S. L. Goldstein (1990), Extreme isotope variations in Heard Island lavas and the nature of mantle reservoirs, *Nature*, *348*, 59–62.
Barling, J., S. L. Goldstein, and I. A. Nicholls (1994), Geochemistry of Heard Island (Southern Indian Ocean): Characterization of an enriched mantle component and implications for enrichment of the sub-Indian ocean mantle, *J. Petrol.*, *35*, 1017–1053.
Becker, T. W., J. B. Kellogg, and R. J. O'Connell (1999), Thermal constraints on the survival of primitive blobs in the lower mantle, *Earth Planet. Sci. Lett.*, *171*, 351–365.
Brandenburg, J. P., E. H. Hauri, P. E. van Keken, and C. J. Ballentine (2008), A multiple-system study of the geochemical evolution of the mantle with force-balanced plates and thermochemical effects, *Earth Planet. Sci. Lett.*, *276*, 1–13, doi:10.1016/j.epsl.2008.08.027.
Cabral, R. A., M. G. Jackson, E. F. Rose-Koga, K. T. Koga, M. J. Whitehouse, M. A. Antonelli, J. Farquhar, J. M. D. Day, and E. H. Hauri (2013), Anomalous sulphur isotopes in plume lavas reveal deep mantle storage of Archaean crust, *Nature*, *496*, 490–494, doi:10.1038/nature12020.
Carbotte, S. M., M. Marjanovic, H. Carton, J. C. Mutter, J. P. Canales, M. R. Nedimovic, S. Han, and M. R. Perfit (2013), Fine-scale segmentation of the crustal magma reservoir beneath the East Pacific Rise, *Nat. Geosci.*, *6*, 866–870, doi:10.1038/NGE01933.
Castillo, P. (1988), The Dupal anomaly as a trace of the upwelling lower mantle, *Nature*, *336*, 667–670.
Chauvel, C., and J. Blichert-Toft (2001), A hafnium and trace element perspective on melting of the depleted mantle, *Earth Planet. Sci. Lett.*, *190*, 137–151.
Christensen, U. R., and A. W. Hofmann (1994), Segregation of subducted oceanic crust in the convecting mantle, *J. Geophys. Res.*, *99*, 19,867–19,884.
Class, C., and A. P. le Roex (2006), Continental material in the shallow mantle—How does it get there?, *Geology*, *34*, 129–132.
Cochran, J. R., J.-C. Sempéré, and S. S. Team (1997), The Southeast Indian Ridge between 88°E and 118°E: Gravity anomalies and crustal accretion at intermediate spreading rates, *J. Geophys. Res.*, *102*, 15,463–15,487.
Donnelly, K. E., S. L. Goldstein, C. H. Langmuir, and M. Spiegelman (2004), Origin of enriched ocean ridge basalts and implications for mantle dynamics, *Earth Planet Sci. Lett.*, *226*, 347–366.
Dosso, L., H. Bougault, P. Beuzart, J.-Y. Calvez, and J.-L. Joron (1988), The geochemical structure of the South-East Indian Ridge, *Earth Planet. Sci. Lett.*, *88*, 47–59.
Doucet, S., D. Weis, J. S. Scoates, V. Debaille, and A. Giret (2004), Geochemical and Hf-Pb-Sr-Nd isotopic constraints on the origin of the Amsterdam-St. Paul (Indian Ocean) hotspot basalts, *Earth Planet. Sci. Lett.*, *28*, 179–195.
Doucet, S., J. S. Scoates, D. Weis, and A. Giret (2005), Constraining the components of the Kerguelen mantle plume: A Hf-Pb-Sr-Nd isotopic study of picrites and high-MgO basalts from the Kerguelen Archipelago, *Geochem. Geophys. Geosyst.*, *6*, Q04007, doi:10.1029/GC2005000806.
Doucet, S., M. Moreira, D. Weis, J. S. Scoates, A. Giret, and C. J. Allègre (2006), Primtive neon and helium isotopic compositions of high-MgO basalts from the Kerguelen Archipelago, Indian Ocean, *Earth Planet. Sci. Lett.*, *241*, 65–79, doi:10.1016/j.epsl.2005.10.025.
Douglas Priebe, L. M. (1998), Geochemical and petrogenetic effects of the interaction of the Southeast Indian Ridge and the Amsterdam-Saint Paul hotspot, MS thesis, 132 pp., Oregon State Univ., Corvallis.
Dupré, B., and C. J. Allègre (1983), Pb-Sr isotope variation in Indian Ocean basalts and mixing phenomena, *Nature*, *303*, 142–146.
Fontignie, D., and J.-G. Schilling (1991), $^{87}Sr/^{86}Sr$ and REE variations along the Easter Microplate boundaries (South Pacific): Application of multivariate statistical analyses to ridge segmentation, *Chem. Geol.*, *89*, 209–241.
French, S., V. Lekic, and B. Romanowicz (2013), Waveform tomography reveals channeled flow at the base of the oceanic asthenosphere, *Science*, *342*, 227–230, doi:10.1126/science.1241514.
Gale, A., S. Escrig, E. J. Gier, C. H. Langmuir, and S. L. Goldstein (2011), Enriched basalts at segment centers: The Lucky Strike (37°17′N) and Menez Gwen (37°50′N) segments of the Mid-Atlantic Ridge, *Geochem. Geophys. Geosyst.*, *12*, Q06016, doi:10.1029/2010GC003446.
Gast, P. W., G. R. Tilton, and C. E. Hedge (1964), Isotopic composition of lead and strontium from Ascension and Gough Islands, *Science*, *145*, 1181–1185.
Goldstein, S. L., G. Soffer, C. H. Langmuir, K. A. Lehnert, D. W. Graham, and P. J. Michael (2008), Origin of a 'southern hemisphere' geochemical signature in the Arctic upper mantle, *Nature*, *453*, 89–94.
Graham, D. W. (2002), Noble gas isotope geochemistry of mid-ocean ridge and ocean island basalts; characterization of mantle source reservoirs, in *Noble Gases in Geochemistry and Cosmochemistry*, edited by D. Porcelli, R. Wieler, and C. J. Ballentine, pp. 247–318, Miner. Soc. Am., Washington, D. C.
Graham, D. W., S. E. Humphris, W. J. Jenkins, and M. D. Kurz (1992), Helium isotope geochemistry of some volcanic rocks from Saint Helena, *Earth Planet. Sci. Lett. 110*, 121–131.
Graham, D. W., P. P. Castillo, J. E. Lupton, and R. Batiza (1996), Correlated helium and strontium isotope ratios in South Atlantic near-ridge seamounts and implications for mantle dynamics, *Earth Planet. Sci. Lett.*, *144*, 491–503.
Graham, D. W., K. T. M. Johnson, L. M. Douglas Priebe, and J. E. Lupton (1999), Hotspot-ridge interaction along the Southeast Indian Ridge near Amsterdam and St. Paul Islands: Helium isotope evidence, *Earth Planet. Sci. Lett.*, *167*, 297–310.
Graham, D. W., J. E. Lupton, F. J. Spera, and D. M. Christie (2001), Upper mantle dynamics revealed by helium isotope variations along the Southeast Indian Ridge, *Nature*, *409*, 701–703.
Graham, D. W., J. Blichert-Toft, C. J. Russo, K. Rubin, and F. Albarede (2006), Cryptic striations in the upper mantle revealed by hafnium isotopes in Southeast Indian Ridge basalts, *Nature*, *440*, 199–202.
Grinsted, A., J. C. Moore, and S. Jevrejeva (2004), Application of the cross wavelet transform and wavelet coherence to geophysical time series, *Nonlinear Processes Geophys.*, *11*, 561–566.
Gurnis, M. (1986a), Quantitative bounds on the size spectrum of isotopic heterogeneity within the mantle, *Nature*, *323*, 317–320.
Gurnis, M. (1986b), Stirring and mixing in the mantle by plate-scale flow: Large persistent blobs and long tendrils coexist, *Geophys. Res. Lett.*, *13*, 1474–1477.
Hamelin, B., and C.-J. Allègre (1985), Large-scale regional units in the depleted upper mantle revealed by an isotope study of the South-West Indian Ridge, *Nature*, *315*, 196–199.
Hamelin, B., B. Dupré, and C.-J. Allègre (1986), Pb-Sr-Nd isotopic data of Indian Ocean ridges: New evidence of large-scale mapping of mantle heterogeneities, *Earth Planet. Sci. Lett.*, *76*, 288–298.
Hammer, O., D. A. T. Harper, and P. D. Ryan (2001), PAST: Paleontological statistics software package for education and data analysis, *Palaeontol. Electron.*, *4*, 9.
Hanan, B., J. Blichert-Toft, D. G. Pyle, and D. M. Christie (2004), Contrasting origins of the upper mantle revealed by hafnium and lead isotopes from the Southeast Indian Ridge, *Nature*, *432*, 91–94.

Hanan, B. B., and D. W. Graham (1996), Lead and helium isotope evidence from oceanic basalts for a common deep source of mantle plumes, *Science*, *272*, 991–995.
Hanan, B. B., and J.-G. Schilling (1989), Easter microplate evolution: Pb isotope evidence, *J. Geophys. Res.*, *94*, 7432–7448.
Hanan, B. B., J. Blichert-Toft, C. Hemond, K. Sayit, A. Agranier, D. W. Graham, and F. Albarede (2013), Pb and Hf isotope variations along the Southeast Indian Ridge and the dynamic distribution of MORB source domains in the upper mantle, *Earth Planet. Sci. Lett.*, *375*, 196–208, doi:10.1016/j.epsl.2013.05.028.
Hanyu, T., and I. Kaneoka (1998), Open system behavior of helium in case of the HIMU source area, *Geophys. Res. Lett.*, *25*, 687–690.
Hanyu, T., I. Kaneoka, and K. Nagao (1999), Noble gas study of HIMU and EM ocean island basalts in the Polynesian region, *Geochim. Cosmochim. Acta*, *63*, 1181–1201.
Hart, S. R. (1984), A large-scale isotope anomaly in the Southern Hemisphere mantle, *Nature*, *309*, 753–757.
Hart, S. R. (1993), Equilibration during mantle melting: A fractal tree model, *Proc. Natl. Acad. Sci. U. S. A.*, *90*, 11,914–11,918.
Hart, S. R., M. Kurz, and Z. Wang (2008), Scale length of mantle heterogeneities: Constraints from helium diffusion, *Earth Planet. Sci. Lett.*, *269*, 507–516.
Harvey, J., A. Gannoun, K. W. Burton, N. W. Rogers, O. Alard, and I. J. Parkinson (2006), Ancient melt extraction from the oceanic upper mantle revealed by Re-Os isotopes in abyssal peridtites from the Mid-Atlantic Ridge, *Earth Planet. Sci. Lett.*, *244*, 606–621.
Hilton, D. R., J. Barling, and G. E. Wheller (1995), Effect of shallow-level contamination on the helium isotope systematics of ocean-island lavas, *Nature*, *373*, 330–333.
Hirschmann, M. M., and E. M. Stolper (1996), A possible role for garnet pyroxenite in the origin of the ''garnet signature'' in MORB, *Contrib. Mineral. Petrol.*, *124*, 185–208.
Hofmann, A. W. (1997), Mantle geochemistry: The message from oceanic volcanism, *Nature*, *385*, 219–229.
Iwamori, H., F. Albarède, and H. Nakamura (2010), Global structure of mantle isotopic heterogeneity and its implications for mantle differentiation and convection, *Earth Planet. Sci. Lett.*, *299*, 339–351, doi:10.1016/j.epsl.2010.09.014.
Janin, M., C. Hemond, M. Maia, P. Nonnotte, E. Ponzevera, and K. T. M. Johnson (2012), The Amsterdam-St. Paul Plateau: A complex hot spot/DUPAL-flavored MORB interaction, *Geochem. Geophys. Geosyst.*, *13*, Q09016, doi:10.1029/2012GC004165.
Janney, P. E., A. P. le Roex, and R. W. Carlson (2005), Hafnium isotope and trace element constraints on the nature of mantle heterogeneity beneath the central Southwest Indian Ridge (13°E to 47°E), *J. Petrol.*, *46*, 2427–2464.
Johnson, K. T. M., D. W. Graham, K. H. Rubin, K. Nicolaysen, D. Scheirer, D. W. Forsyth, E. T. Baker, and L. M. Douglas-Priebe (2000), Boomerang Seamount: The active expression of the Amsterdam-St. Paul hotspot, Southeast Indian Ridge, *Earth Planet. Sci. Lett.*, *183*, 245–259.
Kamenetsky, V. S., R. Maas, N. M. Sushchevskaya, M. D. Norman, I. Cartwright, and A. A. Peyve (2001), Remnants of Gondwanan continental lithosphere in oceanic upper mantle: Evidence from the South Atlantic Ridge, *Geology*, *29*, 243–246.
Katz, R. F., and J. F. Rudge (2011), The energetics of melting fertile heterogeneities within the depleted mantle, *Geochem. Geophys. Geosyst.*, *12*, Q0AC16, doi:10.1029/2011GC003834.
Katz, R. F., and S. M. Weatherley (2012), Consequences of mantle heterogeneity for melt extraction at mid-ocean ridges, *Earth Planet. Sci. Lett.*, *335*, 226–237, doi:10.1016/j.epsl.2012.04.042.
Kellogg, J. B., S. B. Jacobsen, and R. J. O'Connell (2002), Modeling the distribution of isotopic ratios in geochemical reservoirs, *Earth Planet. Sci. Lett.*, *284*, 183–202.
Kellogg, J. B., S. B. Jacobsen, and R. J. O'Connell (2007), Modeling lead isotopic heterogeneity in mid-ocean ridge basalts, *Earth Planet. Sci. Lett.*, *262*, 328–342.
Kingsley, R. H., J. Blichert-Toft, D. Fontignie, and J.-G. Schilling (2007), Hafnium, neodymium, and strontium isotope and parent-daughter element systematics in basalts from the plume-ridge interaction system of the Salas y Gomez Seamount Chain and Easter Microplate, *Geochem. Geophys. Geosyst.*, *8*, Q04005, doi:10.1029/2006GC001401.
Klein, E. M., and C. H. Langmuir (1987), Global correlations of ocean ridge basalt chemistry with axial depth and crustal thickness, *J. Geophys. Res.*, *92*, 8089–8115.
Kogiso, T., K. Hirose, and E. Takahashi (1998), Melting experiments on homogeneous mixtures of peridotite and basalt: Application to the genesis of ocean island basalts, *Earth Planet. Sci. Lett.*, *162*, 45–61.
Kogiso, T., M. M. Hirschmann, and D. J. Frost (2003), High-pressure partial melting of garnet pyroxenite: Possible mafic lithologies in the source of ocean island basalts, *Earth Planet. Sci. Lett.*, *216*, 603–617.
Kurz, M. D., M. Moreira, J. Curtice, D. E. Lott, J. J. Mahoney, and J. M. Sinton (2005), Correlated helium, neon, and melt production on the super-fast spreading East Pacific Rise near 17°S, *Earth Planet. Sci. Lett.*, *232*, 125–142.
Lambart, S., D. Laporte, and P. Schiano (2013), Markers of the pyroxenite contribution in the major-element compositions of oceanic basalts: Review of the experimental constraints, *Lithos*, *160–161*, 14–36, doi:10.1016/j.lithos.2012.11.018.
Langmuir, C. H., and G. N. Hanson (1980), An evaluation of major element heterogeneity in the mantle sources of basalts, *Philos. Trans. R. Soc. London A*, *297*, 383–407.
Lees, J. M., and J. Park (1995), Multiple-taper spectral analysis: A stand-alone C-subroutine, *Comput. Geosci.*, *21*, 199–236.
Liu, C.-Z., J. E. Snow, E. Hellebrand, G. Brügmann, A. von der Handt, A. Büchl, and A. W. Hofmann (2008), Ancient, highly heterogeneous mantle beneath Gakkel ridge, Arctic Ocean, *Nature*, *452*, 311–316.
Lomb, N. R. (1976), Least-squares frequency analysis of unequally spaced data, *Astrophys. Space Sci.*, *39*, 447–462.
Lupton, J., and L. Evans (2004), The atmospheric helium isotope ratio: Is it changing?, *Geophys. Res. Lett.*, *31*, L13101, doi:10.1029/2004GL020041.
Maclennan, J., D. McKenzie, F. Hilton, K. Gronvöld, and N. Shimizu (2003), Geochemical variability in a single flow from northern Iceland, *J. Geophys. Res.*, *108*(B1), 2007, doi:10.1029/2000JB000142.
Mahoney, J., A. P. Le Roex, Z. Peng, R. L. Fisher, and J. H. Natland (1992), Southwestern limits of Indian Ocean Ridge mantle and the origin of low $^{206}Pb/^{204}Pb$ mid-ocean ridge basalt: Isotope systematics of the Central Southwest Indian Ridge (17°–50°E), *J. Geophys. Res.*, *97*, 19,771–19,790.
Mahoney, J. J., J. H. Natland, W. M. White, R. Poreda, S. H. Bloomer, R. L. Fisher, and A. N. Baxter (1989), Isotopic and geochemical provinces of the western Indian Ocean spreading centers, *J. Geophys. Res.*, *94*, 4033–4052.
Mahoney, J. J., J. M. Sinton, M. D. Kurz, J. D. Macdougall, K. J. Spencer, and G. W. Lugmair (1994), Isotope and trace element characteristics of a super-fast spreading ridge: East Pacific Rise, 13–23°S, *Earth Planet. Sci. Lett.*, *121*, 173–193.
Mahoney, J. J., D. W. Graham, D. M. Christie, K. T. M. Johnson, L. S. Hall, and D. L. VonderHaar (2002), Between a hot spot and cold spot: Isotopic variation in the Southeast Indian Ridge asthenosphere, 86°–118°E, *J. Petrol.*, *43*, 1155–1176.
Manga, M. (1996), Mixing of heterogeneities in the mantle: Effect of viscosity differences, *Geophys. Res. Lett.*, *23*, 403–406.

Matsuda, J., T. Matsumoto, H. Sumino, K. Nagao, J. Yamamoto, Y. Miura, I. Kaneoka, N. Takahata, and Y. Sano (2002), The $^{3}He/^{4}He$ ratio of the new internal He Standard of Japan (HESJ), *Geochem. J.*, *36*, 191–195.

Meyzen, C. M., J. Blichert-Toft, J. N. Ludden, E. Humler, C. Mével, and F. Albarède (2007), Isotopic portrayal of Earth's upper mantle flow field, *Nature*, *447*, 1069–1074.

Moreira, M., J. Escartin, E. Gayer, C. Hamelin, A. Bezos, F. Guillon, and M. Cannat (2011), Rare gas systematics on Lucky Strike basalts (37°N, North Atlantic): Evidence for efficient homogenization in a long-lived magma chamber system?, *Geophys. Res. Lett.*, *38*, L08304, doi: 10.1029/2011GL046794.

Nicolaysen, K. P., F. A. Frey, K. T. M. Johnson, J. J. Mahoney, and D. W. Graham (2007), Influence of the Amsterdam/St. Paul hotspot along the Southeast Indian Ridge between 77° and 88°E: Correlations of Sr, Nd, Pb and He isotopic variations with ridge segmentation, *Geochem. Geophys. Geosyst.*, *8*, Q09007, doi:10.1029/2006GC001540.

Olson, P., D. A. Yuen, and D. Balsiger (1984), Convective mixing and the fine structure of mantle heterogeneity, *Phys. Earth Planet. Inter.*, *36*, 591–603.

Parai, R., S. Mukhopadhyay, and J. C. Lassiter (2009), New constraints on the HIMU mantle from neon and helium isotopic compositions of basalts from the Cook-Austral islands, *Earth Planet Sci. Lett.*, *277*, 253–261, doi:10.1016/j.epsl.2008.10.014.

Polvé, M., and C. J. Allègre (1980), Orogenic lherzolite complexes studied by ^{87}Rb-^{87}Sr: A clue to understand the mantle convection processes, *Earth Planet. Sci. Lett.*, *51*, 71–93.

Poreda, R. J., J.-G. Schilling, and H. Craig (1993), Helium isotope ratios in Easter Microplate basalts, *Earth Planet. Sci. Lett.*, *119*, 319–329.

Richter, F. M., and N. M. Ribe (1979), On the importance of advection in determining the local isotopic composition of the mantle, *Earth Planet. Sci. Lett.*, *43*, 212–222.

Rubin, K. H., J. M. Sinton, J. Maclennan, and E. Hellebrand (2009), Magmatic filtering of mantle compositions at mid-ocean ridge volcanoes, *Nat. Geosci.*, *2*, 321–328.

Rudge, J. F., J. Maclennan, and A. Stracke (2013), The geochemical consequences of mixing melts from a heterogeneous mantle, *Geochim. Cosmochim. Acta*, *114*, 112–143, doi:10.1016/j.gca.2013.03.042.

Russo, C. J., K. H. Rubin, and D. W. Graham (2009), Mantle melting and magma supply to the Southeast Indian Ridge: The roles of lithology and melting conditions from U-series disequilibria, *Earth Planet. Sci. Lett.*, *278*, 55–66.

Salters, V. J. M., S. Mallick, S. R. Hart, C. H. Langmuir, and A. Stracke (2011), Domains of depleted mantle: New evidence from hafnium and neodymium isotopes, *Geochem. Geophys. Geosyst.*, *12*, Q08001, doi:10.1029/2011GC003617.

Scargle, J. D. (1982), Studies in astronomical time series analysis. II. Statistical aspects of spectral analysis of unevenly spaced data, *Astrophys. J.*, *263*, 835–853.

Schulz, M., and M. Mudelsee (2002), REDFIT: Estimating red-noise spectra directly from unevenly spaced paleoclimatic time series, *Comput. Geosci.*, *28*, 421–426.

Sempéré, J.-C., J. R. Cochran, and S. S. Team (1997), The Southeast Indian Ridge between 88°E and 118°E: Variations in crustal accretion at constant spreading rate, *J. Geophys. Res.*, *102*, 15,489–15,505.

Shen, Y., and D. W. Forsyth (1995), Geochemical constraints on initial and final depths of melting beneath mid-ocean ridges, *J. Geophys. Res.*, *100*, 2211–2237.

Shorttle, O., and J. Maclennan (2011), Compositional trends of Icelandic basalts: Implications for short–length scale lithological heterogeneity in mantle plumes, *Geochem. Geophys. Geosyst.*, *12*, Q11008, doi:10.1029/2011GC003748.

Small, C., J. R. Cochran, J.-C. Sempéré, and D. M. Christie (1999), The structure and segmentation of the Southeast Indian Ridge, *Mar. Geol.*, *161*, 1–12.

Stracke, A., and B. Bourdon (2009), The importance of melt extraction for tracing mantle heterogeneity, *Geochim. Cosmochim. Acta*, *73*, 218–238, doi:10.1016/j.gca.2008.10.015.

Sun, S.-S., and W. F. McDonough (1989), Chemical and isotopic systematics of oceanic basalts: Implications for mantle composition and processes, in *Magmatism in the Ocean Basins*, edited by A. D. Saunders and M. J. Norry, pp. 313–345, Geol. Soc. Spec. Publ., London.

Tatsumoto, M. (1978), Isotopic composition of lead in oceanic basalts and its implication to mantle evolution, *Earth Planet. Sci. Lett.*, *38*, 63–87.

Thomson, D. J. (1982), Spectrum estimation and harmonic analysis, *Proc. IEEE*, *70*, 1055–1096.

Vlastélic, I., H. Bougault, and L. Dosso (2002), Heterogeneous heat production in the Earth's upper mantle: Blob melting and MORB composition, *Earth Planet. Sci. Lett.*, *199*, 157–172.

White, W. M. (1985), Sources of oceanic basalts: Radiogenic isotopic evidence, *Geology*, *13*, 115–118.

Zindler, A., and S. R. Hart (1986), Chemical geodynamics, *Annu. Rev. Earth Planet. Sci.*, *14*, 493–571.

Zindler, A., E. Jagoutz, and S. L. Goldstein (1982), Nd, Sr and Pb isotope systematics in a three-component mantle: A new perspective, *Nature*, *298*, 519–523.